BONE HEALING

A BMP/activin A chimera is superior to native BMPs and induces bone repair in nonhuman primates when delivered in a composite matrix

Howard J. Seeherman[1]*, Stephen P. Berasi[2], Christopher T. Brown[1], Robert X. Martinez[3], Z. Sean Juo[4], Scott Jelinsky[3], Michael J. Cain[3], Jaclyn Grode[1], Kathleen E. Tumelty[2], Marc Bohner[5], Orly Grinberg[6], Nadav Orr[6], Oded Shoseyov[6], Jeroen Eyckmans[7,8], Christopher Chen[7,8], Pablo R. Morales[9], Christopher G. Wilson[1], Eric J. Vanderploeg[1], John M. Wozney[1]

Bone morphogenetic protein (BMP)/carriers approved for orthopedic procedures achieve efficacy superior or equivalent to autograft bone. However, required supraphysiological BMP concentrations have been associated with potential local and systemic adverse events. Suboptimal BMP/receptor binding and rapid BMP release from approved carriers may contribute to these outcomes. To address these issues and improve efficacy, we engineered chimeras with increased receptor binding by substituting BMP-6 and activin A receptor binding domains into BMP-2 and optimized a carrier for chimera retention and tissue ingrowth. BV-265, a BMP-2/BMP-6/activin A chimera, demonstrated increased binding affinity to BMP receptors, including activin-like kinase-2 (ALK2) critical for bone formation in people. BV-265 increased BMP intracellular signaling, osteogenic activity, and expression of bone-related genes in murine and human cells to a greater extent than BMP-2 and was not inhibited by BMP antagonist noggin or gremlin. BV-265 induced larger ectopic bone nodules in rats compared to BMP-2 and was superior to BMP-2, BMP-2/6, and other chimeras in nonhuman primate bone repair models. A composite matrix (CM) containing calcium-deficient hydroxyapatite granules suspended in a macroporous, fenestrated, polymer mesh–reinforced recombinant human type I collagen matrix demonstrated improved BV-265 retention, minimal inflammation, and enhanced handling. BV-265/CM was efficacious in nonhuman primate bone repair models at concentrations ranging from $^{1}/_{10}$ to $^{1}/_{30}$ of the BMP-2/absorbable collagen sponge (ACS) concentration approved for clinical use. Initial toxicology studies were negative. These results support evaluations of BV-265/CM as an alternative to BMP-2/ACS in clinical trials for orthopedic conditions requiring augmented healing.

INTRODUCTION

Autograft bone is used extensively in orthopedic procedures to augment healing. Limitations of autograft bone include cell viability, cytokine content, available graft volume, donor site morbidity, and increased surgery time (*1*). To address these limitations, bone morphogenetic protein (BMP)/carrier combinations have been developed as bone graft substitutes. BMPs are the only differentiation factors capable of inducing bone after implantation at nonskeletal sites (*2*, *3*) under normal physiological conditions and in multiple species. BMP-2 signaling is required for bone repair in rodents (*4*, *5*) and regulation of bone homeostasis by Wnt (wingless/integrated) (*6*) and parathyroid hormone (*7*).

BMPs consist of two intrachain disulfide bond–stabilized monomers linked into a dimer by an interchain disulfide bond. Canonical Smad (small mothers against decapentaplegic) and noncanonical BMP intracellular signaling initiates in response to BMPs binding to BMP type I and II cell surface receptor complexes. Activated cytoplasmic signaling molecules enter the nucleus and, in the case of bone, regulate transcription of bone-related genes in target precursor cells to initiate bone repair. BMPs, secreted by bone cells and stored within bone extracellular matrix, are released from bone and up-regulated in responding cells after fracture (*2*, *3*). BMP signaling components, present in responding cells, are up-regulated during fracture healing in animal models (*5*, *8*–*11*) and are detected in human fracture callus (*12*). BMP activity is regulated at multiple levels including extracellular inhibitors, cell surface pseudo-receptors, co-receptor activators, and intracellular activators/inhibitors during fracture healing (*2*, *3*, *8*–*12*).

BMP/carrier combinations, extensively investigated in animal models of fracture repair, spine fusion, and oral maxillofacial repair (*13*–*21*), are superior or equivalent to autograft bone in these indications (*16*, *19*–*21*). On the basis of these results, BMP/carrier combinations have been evaluated in clinical trials and subsequently approved for use in humans as bone graft substitutes in all three indications (*22*). Clinical results confirmed BMP/carrier combinations as superior to autograft bone in trauma (*23*) and spine fusion (*22*, *24*) and equivalent to autograft bone in oral maxillofacial indications (*22*). However, to achieve superiority or equivalence to autograft bone, BMPs are often delivered in supraphysiological concentrations. Supraphysiological BMP concentrations have been associated with local adverse events including edema, transient bone resorption, heterotopic bone, and systemic adverse events including increased cancer risk (*25*, *26*). Concerns about increased cancer risk, based on initial small clinical trials (*25*, *26*), have not been observed in multiple larger clinical trials (*25*).

Suboptimal potency/efficacy of singly administered homodimeric or heterodimeric BMPs compared to the mix of naturally occurring cytokines in autograft bone may contribute to the requirement for

[1]Bioventus Surgical, Bioventus LLC, Boston, MA 02215, USA. [2]Centers for Therapeutic Innovation, Pfizer Inc., Boston, MA 02115, USA. [3]Department of Inflammation and Immunology, Pfizer Inc., Cambridge, MA 02139, USA. [4]Biomedical Design, Pfizer Inc., Cambridge, MA 02139, USA. [5]Robert Mathys Stiftung (RMS) Foundation, Bettlach 2544, Switzerland. [6]CollPlant Ltd., Ness Ziona 74140, Israel. [7]Biological Design Center and Department of Biomedical Engineering, Boston University, Boston, MA 02215, USA. [8]Wyss Institute for Biologically Inspired Engineering at Harvard University, Boston, MA 02115, USA. [9]Mannheimer Foundation Inc., Homestead, FL 33034, USA.
*Corresponding author. Email: hseeherman@gmail.com

supraphysiological BMP concentrations. In addition, BMP signaling is complex owing to the dimer nature of the BMP ligands and the requirement for either one or two type I receptors and two type II receptors in a heterohexameric ligand/receptor complex for signal transduction (*27*–*32*). Homodimeric BMPs do not have equipotent receptor binding affinity for BMP type I and II receptors (*28*–*31*). BMP-2 and BMP-4 have higher affinity for BMP type I receptors activin-like kinase-3 (ALK3) and ALK6 than for BMP type II receptors activin receptor type IIA (ACTRIIA), ACTRIIB, and BMP receptor type II (BMPRII). In contrast, BMP-6 and BMP-7 have higher affinity for BMP type II receptors than for BMP type I receptors, although BMP-7 was found to have similar affinity for BMP type I and II receptors in one report (*31*). Heterodimers, composed of BMP-2 and BMP-6 or BMP-7 monomers, combine the receptor binding affinities of their parental BMPs (*32*). Heterodimers retain BMP-2–like high affinity for both type I receptors in the ligand/receptor complex. However, only the BMP-6 or BMP-7 monomer has high affinity for type II receptors. The BMP-2 monomer retains its lower affinity for type II receptors. The improved receptor binding affinity of heterodimers results in increased potency in murine cell–based assays and increased efficacy in rodents compared to BMP-2 or BMP-6 homodimers (*32*). However, the efficacy of heterodimers has not been reported in translational nonhuman primate models of bone repair, critical for determining efficacious BMP doses in human clinical trials (*17*). Extracellular BMP inhibitors may also contribute to the requirement for supraphysiological BMP concentrations. Noggin and gremlin bind BMPs and interfere with BMP receptor binding. Expression of noggin and gremlin is up-regulated by BMPs during fracture healing, suggesting a negative feedback loop limiting efficacy of endogenous BMPs (*2*, *3*, *8*, *9*, *11*, *12*). Lower BMP concentrations required to achieve efficacy in animal models of bone repair and spine fusion compared to nonhuman primate models and human orthopedic clinical trials provide additional evidence for suboptimal BMP efficacy in humans (*14*–*18*, *20*–*22*, *24*, *33*, *34*).

Unexpectedly, homodimeric and heterodimeric BMPs exhibit either weak or no detectable binding to the type I receptor ALK2 based on single receptor/ligand biosensor determinations (*28*, *31*, *35*). ALK2 is the most abundantly expressed BMP type I receptor in primary human bone marrow–derived mesenchymal stem cells (hMSCs) (*36*). Despite the lack of single receptor/ligand biosensor binding, the importance of ALK2 for in vivo BMP signaling is supported by knockdown of ALK2 decreasing osteoblast differentiation of BMP-2–, BMP-4–, BMP-6–, and BMP-7–treated hMSCs (*36*) and osteogenic differentiation of BMP-6–treated mouse endothelial and osteoprogenitor cells (*37*), as well as other mutant mice and cell types (*10*). The importance of ALK2 to bone formation in humans is also supported by the critical role mutations in ALK2 play in the genetic disease fibrodysplasia ossificans progressiva (*10*, *38*). Mutations in the intracellular domain of ALK2 unexpectedly result in activins, normally inhibitors of BMP signaling, inducing ALK2-mediated canonical BMP Smad phosphorylation and associated BMP signaling, leading to excessive bone formation in soft tissues in response to inflammation or soft tissue injury (*38*, *39*).

Rapid release of BMPs and suboptimal presentation of BMPs to cell surface receptors in approved carriers, as well as poor BMP solubility at physiological pH, also contribute to the requirement for increased therapeutic BMP concentrations (*13*, *40*). As a result, initial supraphysiological BMP concentrations appear to be required to maintain physiologic BMP concentrations at the fracture site for a sufficient duration to allow responding cells to accumulate and generate bone repair (*13*). Suboptimal BMP release from approved carriers may also contribute to local adverse events reported with the use of BMPs in orthopedic trauma. Substantial initial burst release of BMP from the approved absorbable collagen sponge (ACS) carrier has been associated with edema, transient bone resorption, and heterotopic bone formation (*13*, *41*). Rapid release of BMP from ACS is the result of higher binding affinity of BMP for serum proteins compared to collagen. Rapid release of BMP from ACS (*13*, *40*, *41*) may also contribute to systemic adverse events.

Two approaches have been proposed to improve the potency/efficacy of BMPs for bone repair. One approach involves BMPs with improved osteogenic potency including heterodimeric BMPs, homodimeric BMP chimeras, and point mutants with improved receptor binding repertoires or resistance to extracellular inhibitors, N-terminal truncated BMPs, and propeptide/BMP complexes (*28*, *42*–*45*). The second approach involves carriers including optimized material/structural properties, extracellular cytokine binding motifs to optimize BMP retention, and synergistic integrin signaling to improve BMP presentation to responding cells (*46*, *47*).

This study combines both approaches to develop a next-generation BMP/carrier that acts as an adjunct to surgical repair of severe open fractures requiring augmented healing. We developed chimeric BMPs engineered for more potent/efficacious bone formation compared to existing BMPs that met the following design criteria: (i) low nanomolar BMP-2–like binding to the ALK3 and ALK6 type I receptors and low nanomolar BMP-6–like binding to the type II receptors ACTRIIA, ACTRIIB, and BMPRII; (ii) increased binding to the ALK2 type I receptor compared to naturally occurring BMPs; and (iii) reduced inhibition by the extracellular BMP antagonists noggin and gremlin and associated picomolar binding to BMP type II receptors. We also engineered a carrier to optimize chimera retention and matrix structure for guided bone repair meeting the following design criteria: (i) chimera retention with minimal initial burst release and prolonged subsequent release similar to the optimized retention of BMP-2 delivered in calcium phosphate matrix (CPM) (*17*), (ii) compression resistance to minimize soft tissue collapse into the repair, (iii) optimized handling properties for multiple surgical indications, (iv) macroporosity to allow guided tissue ingrowth, and (v) biocompatibility and bioresorbability.

Here, we demonstrate that BV-265, a recombinant human BMP-2/BMP-6/activin A chimera, and a composite matrix (CM) consisting of calcium-deficient hydroxyapatite (CDHA) granules suspended in a macroporous, fenestrated, polymer mesh–reinforced recombinant human type 1 collagen (rhCollagen) matrix both met the predetermined design criteria. BV-265 increased BMP intracellular signaling, osteogenic activity, and expression of bone-related genes in murine and human cells to a greater extent than BMP-2 and was not inhibited by BMP antagonist noggin or gremlin. BV-265 induced larger ectopic bone nodules in rats when delivered in buffer, confirming that BV-265 uses BMP signaling components and activates BMP osteogenic target genes in responding cells. BV-265 induced superior bone healing in nonhuman primate bone repair screening models compared to BMP-2, BMP-2/6, and the other chimeras. The combination of BV-265/CM induced ectopic bone in a dose-dependent manner in rats and induced complete healing in translational nonhuman primate bone repair models at concentrations ranging from $^{1}/_{10}$ to $^{1}/_{30}$ of the BMP-2 concentration approved for clinical use in humans. These results support evaluations of BV-265/CM in

human bone repair clinical trials at substantially lower concentrations than are currently approved for BMP-2/ACS.

RESULTS

Chimeric BMPs with enhanced potency/efficacy compared to BMP-2

Homodimeric chimeras were engineered to meet the chimera design criteria by substituting amino acid sequences from recombinant human BMP-6 and recombinant human activin A receptor binding domains into recombinant human BMP-2 (Fig. 1, A to H; fig. S1, A to H; and "Chimera design rationale" section in the Supplementary Materials). Amino acid sequences used to generate the chimeras were chosen to conserve naturally occurring transitions between parental and substituted sequences, minimizing potential immunogenicity. Lead candidates were selected from a larger group of chimeras based on efficacy in cell-based assays and bone formation in rodents (fig. S2).

The BMP-2/BMP-6 chimera, BV-260, was generated by substituting amino acid sequences from β-strands 3, 4, 7, and 8 (involved in BMP type II receptor binding) from BMP-6 to BMP-2 (Fig. 1, A and E, and fig. S1E). Homodimeric BV-260, in contrast to heterodimeric BMPs, exhibited BMP-6–like low nanomolar binding to type II receptors in both monomers while retaining BMP-2–like low nanomolar binding to type I receptors ALK3 and ALK6 (Table 1), meeting the first design criterion. BV-260 had no detectable ALK2 binding similar to BMP-2. Substituting amino acid sequences from the pre-helix loop (PHL) and α-helix 3 (involved in BMP type I receptor binding) from BMP-6 to BMP-2 generate the second BMP-2/BMP-6 chimera BV-261 (Fig. 1, A and F, and fig. S1F). Expressed in mammalian cells, this substitution includes the BMP-6 N-linked glycan. BV-261 demonstrated low nanomolar binding to ALK2, meeting the second design criterion (Table 1). BV-261 retained BMP-2–like low nanomolar binding to ALK3 and ALK6 and BMP-2–like high nanomolar type II receptor binding. ALK2 was the most abundantly expressed BMP type I receptor in human bone ($P < 0.002$) and human muscle ($P < 0.006$), further

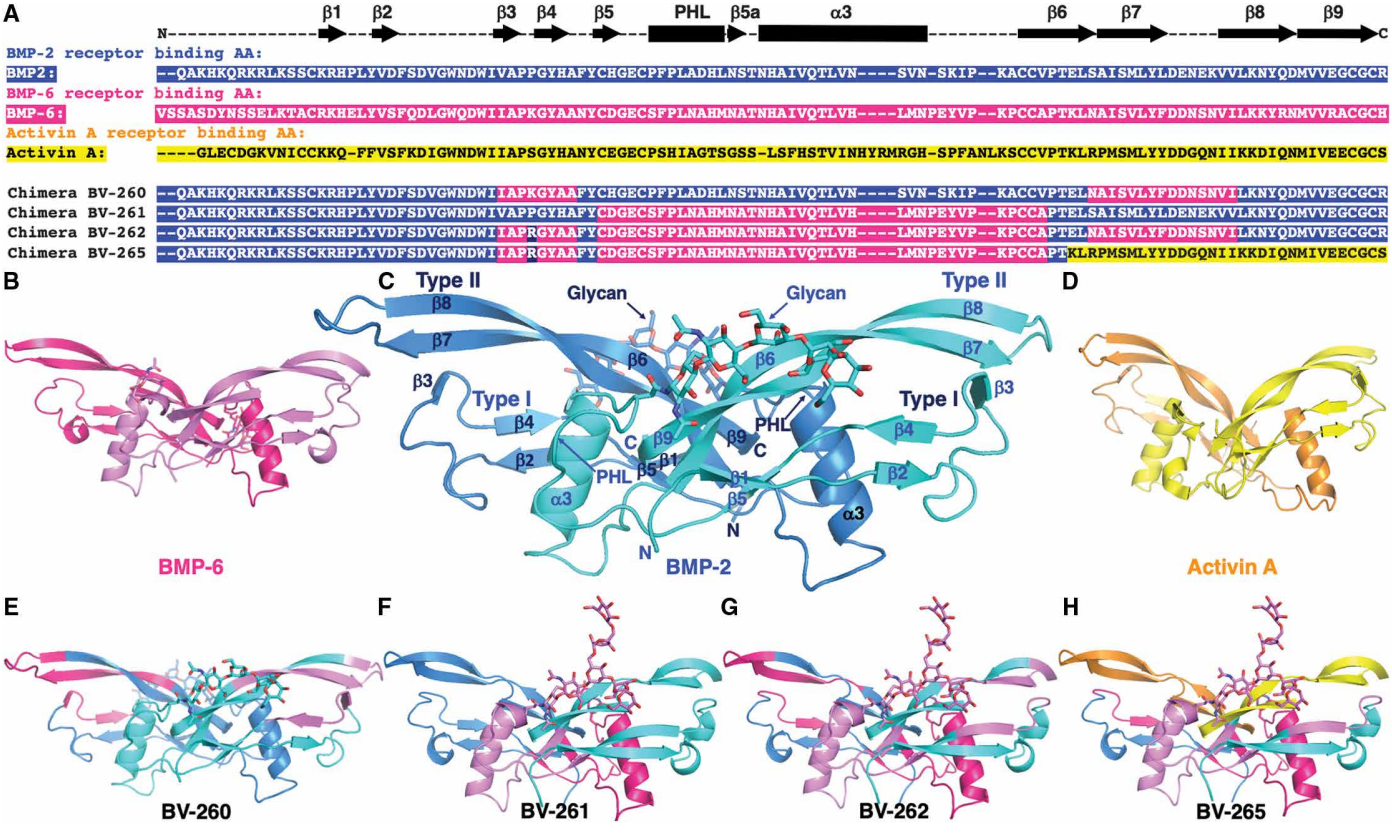

Fig. 1. Amino acid sequence alignment of BMP-2, BMP-6, activin A, and chimera monomers and their corresponding ribbon structures. (**A**) Amino acid (AA) sequence alignment for BMP-2 (blue), BMP-6 (magenta), activin A (yellow), BV-260, BV-261, BV-262, and BV-265 monomers. Amino acid sequences substituted into the chimeras are represented by the corresponding colors of the parental molecules. Positions of β-strands 1 to 9, PHL, and the α-helix 3 (α3) in BMP-2 are located above the amino acid sequence of BMP-2. Ribbon diagrams of glycosylated (**B**) BMP-6 (pink/magenta), (**C**) BMP-2 (cyan/blue), (**D**) activin A (yellow/orange), (**E**) BV-260, (**F**) BV-261, (**G**) BV-262, and (**H**) BV-265 in the "butterfly" orthogonal view. Sections of the chimera ribbon diagrams representing amino acid sequences originating from the BMP-2, BMP-6, and activin A are depicted in the color of the corresponding parental molecule. Labels indicating the location of the type I and II BMP receptor binding domains for each monomer, the relative positions of β-strands 1 to 9 (β1 to β9), the PHL, and the α-helix 3 (α3) are located next to or superimposed on the BMP-2 ribbon diagram (monomer 1, dark blue; monomer 2, blue). Ribbon diagrams of BMP-2, BMP-6, activin A, and BV-261 were generated from the published crystal structure (RCSB Protein Data Bank codes: 6OMN, 6OMO, 2ARV, and 6OML, respectively). The BMP-2 ribbon diagram was used as a surrogate for BV-260. The BV-261 ribbon diagram was used as a surrogate for BV-262 and BV-265. Only one BV-261 monomer displayed a resolved glycan in the crystal structure. The glycan of the second monomer was disordered because of crystal packing artifact. Detailed annotation of the amino acids involved in type I and II receptor binding and glycan tethering can be found in fig. S1A.

Table 1. BMP receptor binding affinity.

Receptor		Receptor binding affinity K_D (nM)								
		BMP-2	BMP-6	BMP-2/6	Activin A	BV-260	BV-261	BV-262	BV-265	TGF-β1
Type 1	ALK1*	–[†]	–	–	–	–	–	NB[‡]	NB	–
	ALK2	NB	700	255	NB	NB	2.2	2.0	0.9	–
	ALK3	1.1	11.0	1.7	NB	1.0	3.3	2.0	1.7	–
	ALK4	–	–	–	–	–	–	NB	NB	–
	ALK5	–	–	–	–	–	–	NB	NB	NB
	ALK6	1.1	20.0	0.5	NB	0.8	0.8	1.0	0.4	–
Type II	ACTRIIA	52.7	3.2	2.5	0.8	2.1	40.0	2.0	<0.1	–
	ACTRIIB	8.0	0.7	1.1	<0.1	0.5	5.0	0.5	<0.1	–
	BMPRII	26.7	3.9	8.0	1.3	3.6	82.0	3.5	<0.1	–
	TBRII	–	–	–	–	–	–	NB	NB	<0.1

*BMP-9–positive control K_D for ALK1 = 0.5 nM. †Not performed. ‡NB = no specific binding (>200 nM).

supporting the inclusion of increased ALK2 binding in the design criteria (fig. S3 and "Species specific BMP receptor expression" section in the Supplementary Materials).

BV-262 was generated from BV-260 and BV-261, combining their associated BMP-6 amino acid substitutions into BMP-2 in a single chimera (Fig. 1, A and G, and fig. S1G). BV-262 retained the BV-260– and BMP-6–like low nanomolar binding to BMP type II receptors, the BV-261–like low nanomolar binding to ALK2, and the BMP-2–like low nanomolar binding to ALK3 and ALK6 (Table 1). Last, a BMP-2/BMP-6/activin A chimera, BV-265, was generated by substituting the C-terminal β-strands 6, 7, 8, and 9 (involved in type II receptor binding) from activin A to BV-262 (Fig. 1, A and H, and fig. S1H). This substitution results in BV-265 exhibiting reduced inhibition by extracellular BMP antagonists noggin and gremlin (confirmed below) and associated picomolar binding for the shared BMP/activin A type II receptors ACTRIIA and ACTRIIB similar to activin A (Table 1). The combination of these two attributes meets the third design criterion. BV-265 also demonstrated optimized binding to all BMP receptors as a result of combining design criteria 1 and 2 from BV-262 with design criterion 3 into a single chimera. Consistent with this observation, BV-265 demonstrated no detectable biosensor binding to the activin A type I receptor ALK4, transforming growth factor–β (TGF-β) type I receptor ALK5, TGF-β type II receptor TGF-β type II (TβRII), or the BMP-9 type I receptor ALK1 as did BV-262. BV-265 and the other chimeras share the BMP-2 N termini responsible for interactions with heparinic sites in extracellular matrix and on cell surfaces (*48*). As a result, BMP-2 and the chimeras have similar heparin binding affinity (fig. S4).

Tethered glycans are responsible for increased BV-261 versus BMP-6/ALK2 binding

The BMP-2, BMP-6, and BV-261 crystal structures revealed key differences in the pattern of glycosylation and associated PHL and α-helix 3 region confirmation/flexibility reported to be determinants for BMP type I receptor binding (*29*, *35*, *49*–*51*). The tethered BMP-6 N-linked glycan, confirmed below to be critical for increased ALK2 binding by deglycosylation, was responsible for increased BV-261/ALK2 binding compared to BMP-6.

Four unique copies of the glycosylated BMP-2 monomer resolved in the crystal lattice, each under a different crystallographic environment (fig. S5A and table S1). An N-linked glycan at position N56, located between the PHL and α-helix 3, was clearly defined containing numerous perfectly ordered and precisely positioned monosaccharides along the surface of the four BMP-2 copies. Despite some flexibility within the attached PHL/α-helix 3 and the finger regions, the first four glycan monosaccharides were structurally well aligned among all four BMP-2 copies.

The N-linked glycan is attached to the surface of BMP-2 by a pair of "glycan tethers" generated from an extensive network of hydrogen bonds between the surface residues R16 and E109, the second *N*-acetyl-D-glucosamine (GlcNAc), β-D-mannose, and a branching α-D-mannose (Fig. 2A). The tethered glycan has the potential to alter the flexibility/conformation of the attached PHL/α-helix 3 region involved in BMP type I receptor binding (fig. S5A) and to increase BV-261/ALK2 binding. Flexibility/conformation of this region plays an important role in the "induced fit" mechanism of BMP/receptor binding, allowing adaptation of the ligand to the varied surface topography of their receptor binding partners (*35*, *51*, *52*). Despite the presence of a similar tethered glycan and the favorable PHL/α-helix 3 flexibility/conformation, glycosylated BMP-2 does not bind to ALK2 with detectable affinity in single receptor/ligand biosensor determinations (Table 1).

Two unique copies of the glycosylated BMP-6 monomer resolved in the crystal lattice, each having a largely disordered glycan with only two traceable glycan monosaccharides (fig. S5B). The K40 and R134 surface residues of BMP-6 in the corresponding positions of the BMP-2 R16 and E109 glycan tethers do not elicit sufficient hydrogen bonding to form glycan tethers due to structural constraints. In contrast to BMP-2, the two copies of BMP-6 have very different PHL conformations due, in part, to increased mobility resulting from the lack of a tethered glycan. BMP-7 contains the same K40 and R134 surface residues that prevent glycan tethering in BMP-6 and binds ALK2 with similar weak micromolar affinity based on single receptor/ligand biosensor determinations (*30*, *35*). Despite this weak interaction, BMP-6 and BMP-7 have been reported

to preferentially signal through ALK2 (*30*, *35*, *36*).

The crystal structure of BV-261 contains a dimer in each asymmetric unit (Fig. 1F). The N-linked glycan on one BV-261 monomer was disordered because of crystal contact. However, the other monomer contained a fully resolved glycan without any crystal packing artifact and was selected for structural analysis. BV-261 retains the R16 and E109 glycan tethers inherited from the BMP-2 finger regions (Fig. 2B), resulting in the BV-261 glycan being firmly attached to the protein surface. Superimposition of BV-261 on BMP-2 and BMP-6 demonstrated that tethered BV-261 N-linked glycan/PHL region derived from BMP-6 adopts a conformation similar to the tethered BMP-2 N-glycan/PHL region, very different from the highly mobile BMP-6 nontethered N-glycan/PHL region (Fig. 2, C and D). BV-262 also inherits the R16 and E109 glycan tethers from BMP-2, whereas BV-265 inherits the R16 glycan tether from BMP-2 and E109 glycan tether from activin A (Fig. 1A). BV-261, BV-262, and BV-265 bind ALK2 with high affinity, in contrast to BMP-2 and BMP-6 (Table 1).

Glycosylation is reported to play a critical role in the weak single receptor/ligand biosensor BMP-6/ALK2 binding (*35*). BMP-6/ALK3 and ALK6 binding was not affected by deglycosylation, indicating an independent mechanism for these interactions. BV-261/ALK2 binding is also dependent on glycosylation. Partial deglycosylation with Endo H_f, confirmed by SDS–polyacrylamide gel electrophoresis (SDS-PAGE) (fig. S6A), substantially diminished BV-261/ALK2 binding (K_D = 2.2 to 458 nM; fig. S6, B and C) to a K_D similar to BMP-6 (Table 1). Partial deglycosylation with Endo H_f cleaves the glycan between the first and second GlcNAc monosaccharides, eliminating the glycan tether, but leaves the first GlcNAc monosaccharide, critical for BMP-6/ALK2 binding, attached (*35*). Similar to BMP-6, deglycosylation did not affect BV-261/ALK6 binding compared to glycosylated BV-261 (K_D = 1 nM for both conditions; fig. S6, D and E). Consistent with decreased BV-261/ALK-2 binding, potency of ALP activity in C2C12 cells treated with Endo H_f partially deglycosylated BV-261 was reduced compared to fully glycosylated BV-261 (Fig. 2E). Similar partial deglycosylation of BMP-2 resulted in only a small decrease in potency.

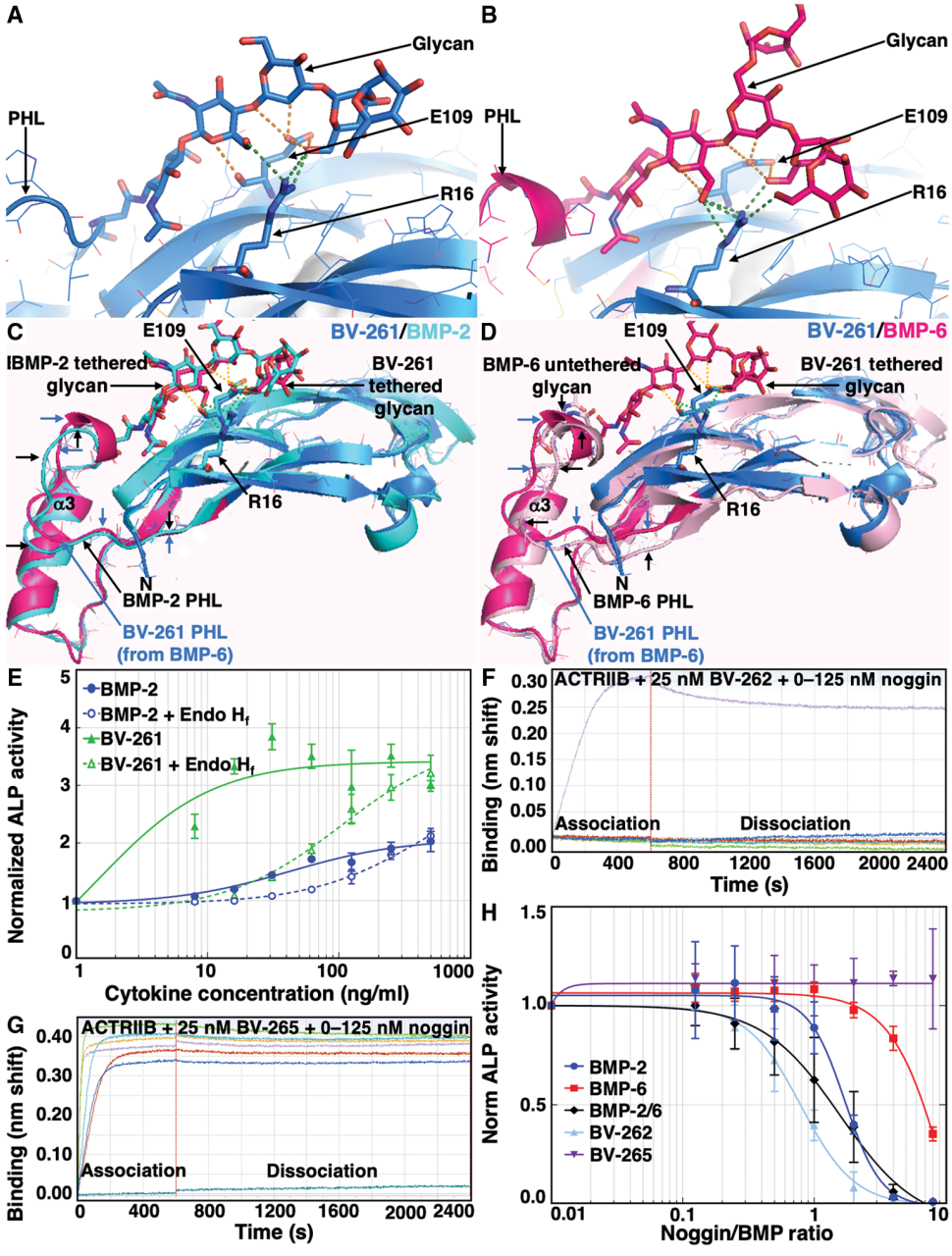

Fig. 2. Structural and cell-based support for increased BV-261/AKL2 binding due to glycan tethering and the effect of noggin on ACTRIIB/BMP/chimera binding and ALP activity. (**A**) Magnified ribbon diagram of BMP-2 and (**B**) BV-261 demonstrating glycan tethering by R16 and E109 (hydrogen bonds represented by green and orange dotted lines, respectively). (**C**) Ribbon diagram of a BV-261 monomer composed of amino acid sequences from the PHL and α3 helix regions of BMP-6 (red) substituted into BMP-2 (blue; Fig. 1, A and F) superimposed on BMP-2 (cyan) and (**D**) BMP-6 (pink). The position of the PHL of BV-261 compared to BMP-2 or BMP-6 is indicated by the blue and black arrows, respectively. The position of the N terminus is designated by N. (**E**) Alkaline phosphatase (ALP) activity in C2C12 cells as a function of BMP-2, endoglycosidase H (Endo H_f)–treated BMP-2, BV-261, and Endo H_f–treated BV-261 concentration (n = 3 and 2 repetitions per plate). (**F**) Sensorgrams comparing BV-262 (25 nM) and (**G**) BV-265 (25 nM) binding to ACTRIIB immobilized on the biosensor (nanometer shift) as a function of noggin concentration (0.125 nM). (**H**) ALP activity in C2C12 cells after treatment with BMP-2, BMP-6, BMP-2/6, BV-262, or BV-265 in the presence of increasing noggin concentration (n = 3 and 2 repetitions per plate). Data are means ± SD (data file S1).

These results confirm that the tethered glycan is directly involved in the mechanism responsible for increased BV-261/ALK2 binding compared to BMP-6 and BMP-7, both lacking glycan tethers. However,

a tethered glycan alone cannot explain the difference between BV-261 and BMP-2/ALK2 binding because both proteins have similarly tethered glycans. In the absence of the cocrystal structure of the BV-261/ALK2 complex, additional potential mechanisms contributing to this difference including differences in the charge interaction between the putative BV-261 and BMP-2 ALK2 binding surfaces are discussed in the "Alternative mechanisms for increased ALK2 binding" section in the Supplementary Materials and fig. S7.

Reduced BV-265 noggin/gremlin inhibition is due to more favorable picomolar BV-265/type II binding

Similar to other BMPs, BV-262 binds noggin with high affinity (K_D = 15 pM; fig. S8A), and the presence of noggin inhibits BV-262/ACTRIIB binding (Fig. 2F). As previously reported (*45*), activin A does not bind noggin (K_D > 1000 nM; fig. S8B). Despite the presence of the activin A C-terminal amino acid sequence in the second finger region involved in BMP/noggin binding, BV-265 also binds noggin but at a much lower affinity than BMPs and BV-262 (K_D = 3.0 nM; fig. S8C). In contrast to BMPs and BV-262, there is a strong association between BV-265 and ACTRIIB at noggin concentrations up to 125 nM (Fig. 2G). This strong association is likely due to the picomolar binding affinity of BV-265 for the BMP type II receptors favoring ACTRIIB/receptor binding over nanomolar binding affinity of BV-265 for noggin. Inability to inhibit BV-265/ACTRIIB binding translated to a lack of noggin inhibition of ALP activity in C2C12 cells treated with BV-265 at noggin concentrations evaluated in the assay (Fig. 2H). In contrast, noggin inhibited BMP-2–, BMP-6–, BMP-2/6–, and BV-262–induced ALP activity. Gremlin inhibited BMP-2– and BMP-2/6–induced, but not BV-265–, BV-262–, and BMP-6–induced, ALP activity in C2C12 cells (fig. S8D). Gremlin differs in structure and mechanism of BMP inhibition compared to noggin (*53*).

Activity in murine and human cell-based assays and rodent intramuscular implants confirms that chimeras signal primarily through BMP pathways

Murine C2C12 cells express mRNA for ALK2, ALK3, ACTRIIA, BMPRII, and low amounts of ALK6 and ACTRIIB (*31*). BV-265 induced greater phospho–Smad 1/5 (pSmad 1/5) and phospho–p-38 (pp38) activation in C2C12 cells at 30 min compared to treatment with BMP-2 (fig. S9, A to C). Consistent with the lack of ALK4, ALK5, and TβRII receptor binding, both cytokines induced minimal activin A/TGF-β–like activation of pSmad 3 compared to TGF-β1 (fig. S9D).

hMSCs express a similar repertoire of BMP receptors to C2C12 cells, with the exception of ALK2 being the most abundantly expressed BMP type I receptor (*36*). pSmad 1/5 and pp38 were induced earlier and to a greater extent in BV-265–treated hMSCs compared to BMP-2 (fig. S10, A to F). Both cytokines induced minimal pSmad 3 activity compared to TGF-β1 (fig. S10G).

Human periosteal derived stem cells (hPDCs) express mRNA for ALK2, ALK3, and BMPRII (fig. S11A). Receptor mRNA expression was not up-regulated in response to 14 days of treatment with BMP-2, BV-262, or BV-265. Activation of pSmad 1/5/8 and pp38 was similar after 24 hours of treatment with BMP-2, BMP-2/6, BV-262, or BV-265 (100 ng/ml) (fig. S11, B to E). Minimal activation of pSmad 3 was detected (fig. S11, F and G, and table S1). Small interfering RNA (siRNA)–mediated ALK2 knockdown resulted in a substantial decrease in activation of pSmad 1/5/8 and pp38 in response to treatment with all four cytokines. Decreased expression of ALK2, but not ALK3 or BMPRII, confirmed specific siRNA-mediated ALK2 knockdown compared to siRNA-scramble (fig. S11H). siRNA-mediated knockdown of ALK2 and/or ALK3 also reduced pSmad 1/5 activation in BMP-2– and BMP-2/6–treated hMSCs (fig. S11I). These results, as well as previous reports (*36*, *37*), support the key role of BMP and chimera/ALK2 signaling in vivo, independent of ex vivo single receptor/ligand biosensor measurements of ALK2 binding affinity (Table 1).

Consistent with the lack of BMP and chimera binding to activin A type I receptors, TGF-β type I and II receptors, and the lack of pSmad 2/3 activation, downstream activation of the activin A/TGF-β Smad 2/3–responsive cytotoxin-associated gene A (CAGA)–luciferase reporter was not observed in BMP-2–, BV-262–, or BV-265–treated C2C12 cells (fig. S12A). As expected, signaling was observed in response to TGF-β1 treatment. BMP activation of Smad 2/3–mediated TGF-β signaling through hybrid BMP/TGF-β receptor complexes has been reported in embryonic and transformed cell lines (*54*). Downstream TGF-βSmad 3/4–inducible soluble embryonic alkaline phosphatase (SEAP) reporter activation was observed in BV-265– and BMP-2–treated human embryonic kidney (HEK-Blue TGF-β) cells but only at substantially higher concentrations compared to TGF-β (fig. S12B).

The percentage of cells exhibiting positive nuclear staining for Smad 1/5/8 was greater in explants treated with BMP-2 (5.0 mg) or BV-262/ACS (0.5 mg or 5.0 mg), but not BMP-2/ACS (0.05 mg), compared to treatment with buffer/ACS (fig. S13, A to F). The presence of in vivo BMP-2 and BV-262 Smad 1/5/8 signaling supports the in vitro characterization of chimera BMP signaling and, in addition to bone formation, confirms BMP signaling in responding cells.

Chimeras induce both early- and late-stage osteogenic activity in cell-based assays

Potency of ALP activity, an indicator of early-stage osteoblast differentiation, estimated by the median effective concentration (EC_{50}) was greater in murine C2C12 cells treated with BMP-2/6, BV-262, BV-261, or BV-265 compared to BMP-2 (Fig. 3A). BV-260, BMP-6, and BMP-2 had similar EC_{50} values. Efficacy, determined from the plateau in ALP activity versus cytokine concentration, was similar in all treatments. Increased activity of the current BMP-2/6 formulation compared to BMP-2 and BMP-6 was confirmed, similar to previously reported BMP-2/6 formulations (fig. S14 and "Comparative efficacy of BMP-2/6 formulations" section in the Supplementary Materials) (*32*). BV-265 induced mineralization, an indicator of late-stage osteoblast differentiation, in C3H10T$^1/_2$ cells at lower concentrations compared to BV-262 and BMP-2 (Fig. 3B).

mRNA expression of ALP, SYR-box 9 (SOX9), osterix (OSX), and runt-related transcription factor 2 (RUNX2) was used to compare early-stage osteoblast differentiation in hPDCs in response to treatment with BMP-2, BMP-2/6, BV-262, or BV-265 for 2 weeks. ALP and SOX9 mRNA expression were significantly greater in hPDCs treated with BV-265 compared to BV-262, BMP-2, or BMP-2/6 (Fig. 3C). Increased OSX mRNA expression in response to treatment with BV-265 was similar to BV-262 and BMP-2/6 and greater than BMP-2. Increased RUNX2 mRNA expression induced by BV-265 was similar to BMP-2/6 and was significantly greater than BV-262 and BMP-2. BV-265, BV-262, and BMP-2/6 induced similar ALP activity (Fig. 3D). ALP activity induced by BV-265 and BMP-2/6 was significantly greater than BMP-2. ALP activity induced by all cytokines was greater than growth media alone. Only BV-265 (100 ng/ml) induced mineralization in hPDCs, indicative of late-stage osteoblast differentiation (Fig. 3E).

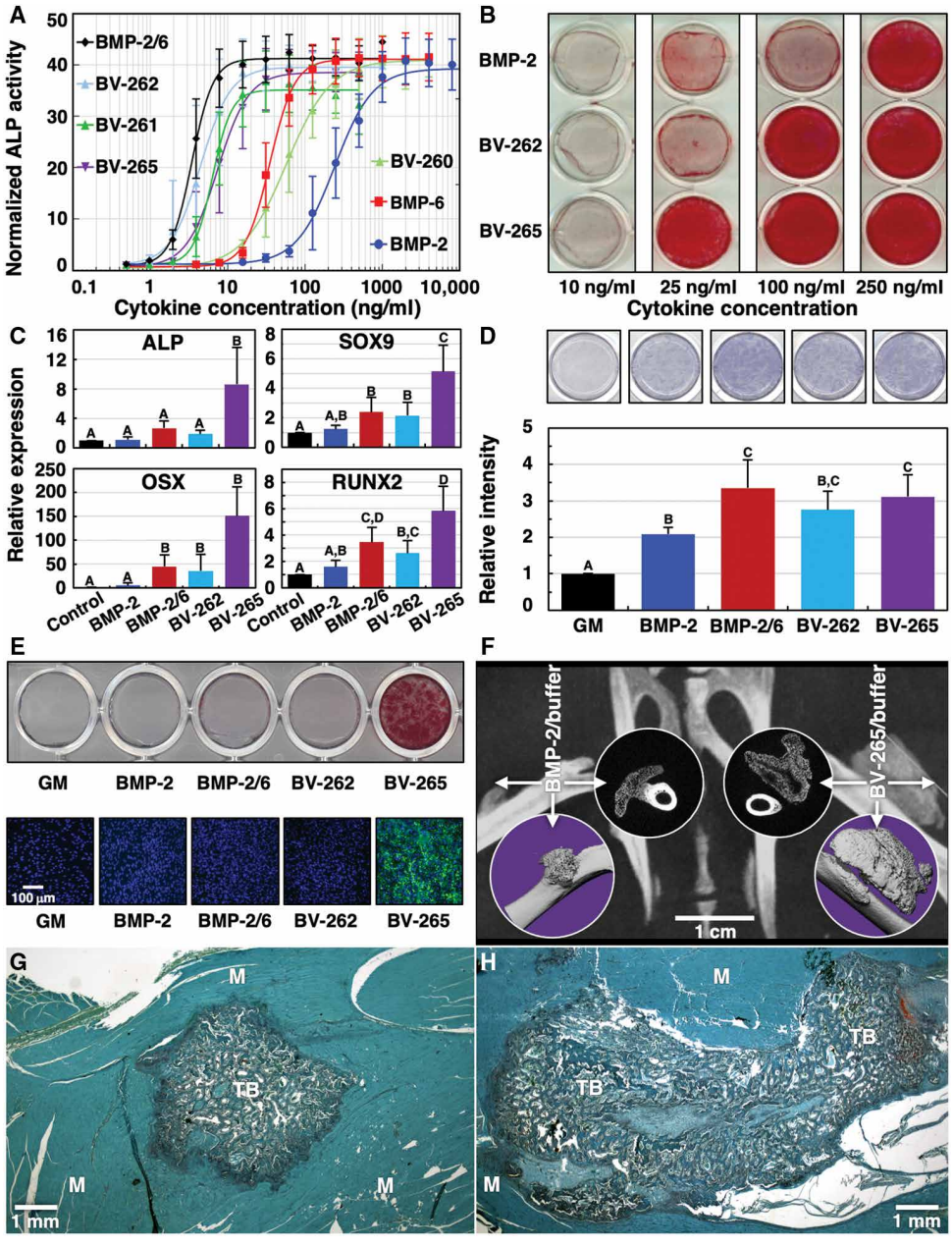

Fig. 3. Comparison of BMPs and chimeras in cell-based and rodent bone induction assays. (**A**) ALP activity in C2C12 cells as a function of BMP and chimera concentration. Data are means ± SD ($n = 3$ repetitions of duplicate determinations). Mean values for EC_{50}: BMP-2 = 4 ± 1 ng/ml^{D}, BV-262 = 5 ± 3 ng/ml^{B,D}, BV-261 = 7 ± 1 ng/ml^{B,C,D}, BV-265 = 8 ± 3 ng/ml^{B,C,D}, BV-260 = 61 ± 20 ng/ml^{A,C}, BMP-6 = 36 ± 68 ng/ml^{A,B}, and BMP-2 = 257 ± 99 ng/ml^{A}. Mean values for EC_{50} not sharing the same letter are significantly different [Kruskal-Wallis rank sum test group effect, $P > 0.0001$; Dunn post hoc test, $P < 0.05$ (group comparison P values in data file S1)]. (**B**) Mineralization of C3H10T$^{1}/_{2}$ cells as a function of BMP-2, BV-262, and BV-265 concentration after 10 days ($n = 3$). (**C**) mRNA expression of *ALP*, *SOX9*, *OSX*, and *RUNX2* normalized to glyceraldehyde-3-phosphate dehydrogenase (GAPDH) in hPDCs induced by growth media (GM), BMP-2, BMP-2/6, BV-262, and BV-265 (100 ng/ml) after 14 days determined by reverse transcription polymerase chain reaction (RT-PCR). (**D**) ALP activity in hPDCs after 14 days of stimulation by growth media, BMP-2, BMP-2/6, BV-262, and BV-265 (100 ng/ml; top, fast blue stained wells; bottom, relative staining intensity; $n = 4$). Mean values not sharing the same letter are significantly different [analysis of variance (ANOVA) group effect, $P < 0.0002$ and 0.0001, respectively; Tukey honestly significant difference (HSD) post hoc test, $P < 0.05$ (group comparison P values in data file S1)]. (**E**) Mineralization of hPDCs 23 days after stimulation with BMP-2, BV-262, or BV-265 (100 mg/ml) (top, Alizarin red–stained wells; bottom, Osteolmage-stained wells; $n = 4$). (**F**) Radiographs and μCT 3D and slice images of bone induction 16 days after injection of either BMP-2/buffer or BV-265/buffer (0.22 mg each) into muscle adjacent to the femur in rats ($n = 4$). (**G**) Histological appearance of a BMP-2/buffer–treated and (**H**) a BV-265/buffer–treated intramuscular explant demonstrating a bone nodule within the surrounding muscle (M) consisting of trabecular bone (TB) within highly vascularized connective tissue 16 days after injection (Safranin-O/Fast Green stain). Higher-magnification images in figs. S17 to S19. Individual data can be found in data file S1.

Chimeras regulate bone-endothelial cross-talk

BMPs have been reported to regulate bone-endothelial cell cross-talk required for formation of the vasculature critical for bone formation and differentiation of osteogenic precursors from vascular-derived cells (*3*, *55*). BMP-2, BMP-2/6, BV-262, and BV-265 failed to up-regulate vascular endothelial growth factor-A (VEGF-A) mRNA expression but increased secreted VEGF-A protein in hPDCs compared to control under the conditions evaluated (fig. S15, A and B). BMP-2/6, BV-262, and BV-265, but not BMP-2, induced VEGF-A mRNA expression in human microvascular endothelial cells (hMVECs). Tip- and stalk-associated gene expression was not up-regulated by BMPs or chimeras in hMVECs under the conditions tested (fig. 15, C and D). BMP-2, BV-262, and BV-265 induced minimal BMP receptor expression, pSmad 1/5/8 activation, early osteogenic gene expression, and ALP activity in human endothelial cells (fig. S16, A to F). A more detailed characterization of BMP/chimera endothelial cross-talk can be found in the "Chimera/bone-endothelial cross-talk" section in the Supplementary Materials.

BV-265/buffer induces larger intramuscular bone nodules in rats compared to BMP-2

Intramuscular injection of BV-265/buffer (0.22 mg), independent of a carrier, induced significantly larger radiodense nodules compared to contralateral injection of BMP-2/buffer (0.22 mg) in rats (237.3 ± 21.7 mm^3 versus 59.7 ± 18.7 mm^3, respectively; $P < 0.02$;

Fig. 3F). Histology confirmed the presence of peripheral de novo trabecular bone formed by a combination of direct and endochondral pathways, depending on the degree of vascularization, in both treatment groups (Fig. 3, G and H, and figs. S17 to S19). The central region contained woven trabecular bone undergoing secondary lamellar remodeling within a highly vascularized, cellular connective tissue. The bone nodules contained centrally located regions of large branching sinusoidal vessels consistent with rapid initial vascularization, whereas peripheral regions contained smaller circumscribed vessels (figs. S20 and S21). Blood vessel area fraction was significantly greater in regions of large sinusoidal vessels compared to regions with smaller circumscribed vessels (BV-265/buffer = 28.2 ± 1.6% and BMP-2/buffer = 24.9 ± 4.3% versus BMP-265/buffer = 10.6 ± 1.7% and BMP-2/buffer = 7.8 ± 2.1%, respectively; $P > 0.002$, equal variance two-tailed paired t test; data file S1). Vessel area fractions for each region were similar in response to both treatments ($P = 0.27$). Increased vasculature was also visible within the transition zone between the periphery of the bone nodule and the surrounding muscle.

BV-265 induces superior bone repair at lower concentrations compared to BMPs and other chimeras in macaque fibula osteotomy screening models

Macaque fibula osteotomy models were used to compare the efficacy of BMP-2/6 or the chimeras to BMP-2 and to select the lead chimera for additional translational evaluation. Nonhuman primates were selected on the basis of publications supporting translation of efficacious BMP-2 concentrations in nonhuman primate models of bone repair and spine fusion to efficacy in human clinical trials compared to other animal species (*17*, *20*, *22*, *34*). Efficacy was evaluated at 0.5 mg/cm^3 of carrier, one-third the BMP-2/ACS concentration (1.5 mg/cm^3) approved for clinical use, based on the increased potency/efficacy of BMP-2/6 and the chimeras compared to BMP-2 in cell-based and rodent bone induction assays. Details of the nonhuman primate fibula osteotomy models, rationale for the selected models, and specific cytokine carriers can be found in the "NHP osteotomy model characterization" section in the Supplementary Materials and in published reports (*17*, *56*). A detailed description of the efficacy of the BMPs and chimeras in the NHP fibula osteotomy screening models can be found in the "BMP/chimera NHP fibula osteotomy screening results" section in the Supplementary Materials, data file S1, and table S2.

Despite BMP-2/6 having a superior BMP receptor binding affinity repertoire (Table 1) and increased efficacy in cell-based and rodent bone induction assays (fig. S14) (*32*), treatment with BMP-2/6/ACS or BMP-2/ACS (0.5 mg/cm^3) resulted in similar poor radiographic, micro–computed tomography (μCT), callus volume, mechanical testing, and histological outcomes (Fig. 4, A and B; fig. S22A; and Table 2) at 10 weeks. The inability to accelerate repair at substantially lower concentrations indicates that BMP-2/6 may not be a more efficacious alternative to BMP-2 in human bone repair indications. Poor radiographic, μCT, callus volume, and mechanical testing outcomes were also observed in response to treatment with BMP-2 or BV-260/ACS (0.5 mg/cm^3) at 8 weeks despite low nanomolar BMP type I and II receptor binding affinity of both BV-260 monomers compared to BMP-2/6 (Fig. 4, C and D, and Table 2). The addition of ALK2 binding in BV-261 resulted in accelerated and increased callus formation in the BV-261/ACS–treated fibula osteotomies (0.5 mg/cm^3) compared to contralateral BMP-2/ACS–treated osteotomies (0.5 mg/cm^3) at 8 weeks. However, radiographic, μCT, and biomechanical outcomes remained poor in response to both treatments (Fig. 4, E and F, and Table 2).

Combining low nanomolar BMP type I and II receptor binding affinity of BV-260 and increased ALK2 binding from BV-261 into a single chimera resulted in BV-262/ACS–treated osteotomies (0.5 mg/cm^3), demonstrating accelerated radiographic and μCT repair (Fig. 4, G and H), as well as better histological (fig. S22B) and biomechanical (Table 2) outcomes compared to contralateral BMP-2/ACS–treated osteotomies (0.5 mg/cm^3) at 10 weeks. Torsional stiffness of the BV-262/ACS–treated osteotomies approached the value for intact fibulae, and maximum torque was similar to intact fibulae.

The efficacy of BV-262 (0.5 mg/cm^3) was then compared to BMP-2 (1.5 mg/cm^3) to determine whether the reduced BV-262 concentration induced similar outcomes to BMP-2 delivered at the concentration of BMP-2/ACS approved for clinical use in humans. CPM was selected as the carrier to eliminate the central radiolucent region observed within the developing callus in response to rapid peripheral bone formation induced by BV-262/ACS. CPM has a substantially lower initial burst release of BMP and prolonged subsequent BMP release compared to ACS (*17*). Both treatments resulted in similar radiographic, μCT, histological (Fig. 5, A to C), and biomechanical outcomes (Table 2). These results suggest that BV-262 is as effective as BMP-2 in enhancing bone repair at one-third the concentration.

Combining the low nanomolar binding affinity for all BMP type I receptors, including ALK2, from BV-262 with decreased inhibition by extracellular BMP antagonists noggin and gremlin and the associated picomolar BMP type II receptor binding into a single chimera resulted in BV-265/CPM (0.5 mg/cm^3) inducing similar radiographic, μCT, and histological outcomes to the contralateral BV-262/CPM–treated osteotomies (0.5 mg/cm^3) at 8 weeks (Fig. 5, D to F). However, BV-265/CPM–treated osteotomy torsional stiffness was 37.4% greater than the contralateral BV-262/CPM–treated osteotomies and approached the value for intact fibulae (Table 2). Maximum torque was 54.7% greater in BV-265/CPM–treated osteotomies compared to BV-262/CPM and was similar to the value for intact fibulae. BV-265 was selected as the lead chimera for additional translational studies based on superior in vitro and in vivo results compared to BMP-2, BMP-2/6, and the other chimeras.

Carrier with optimized chimera retention and matrix properties

The CM consists of 0.4- to 0.8-mm CDHA granules suspended in a rhCollagen matrix engineered with 50- to 250-μm interconnected pores (Fig. 6, A to C). The CM also was fabricated with an array of 1.5-mm fenestrations and is reinforced with a poly(glycolide-*co*-lactide) (PGLA) copolymer mesh. The top and bottom surfaces of the CM were coated with a thin layer of rhCollagen alone. The CDHA granules were designed with high specific surface area (>50 m^2/g) and 10- to 20-μm interconnected pores to enhance cytokine binding throughout the granules (Fig. 6, D and E). The fenestrations also facilitate uniform distribution of the BV-265/buffer solution to the CDHA granules in the CM during initial cytokine loading. Fluorescence microscopy of sectioned granules confirmed that Alexa Fluor 488–conjugated BV-265 was present on the surface and in the interior of the CDHA granules (Fig. 6F).

The retention profile, half-life ($t_{1/2}$), and area under the curve (AUC) for ^{125}I-labeled BV-265/CM after implantation in a rat muscle pouch were similar to ^{125}I-labeled BMP-2/CPM and superior to BMP-2/ACS and BMP-2/buffer, meeting the first design criterion (Fig. 6G

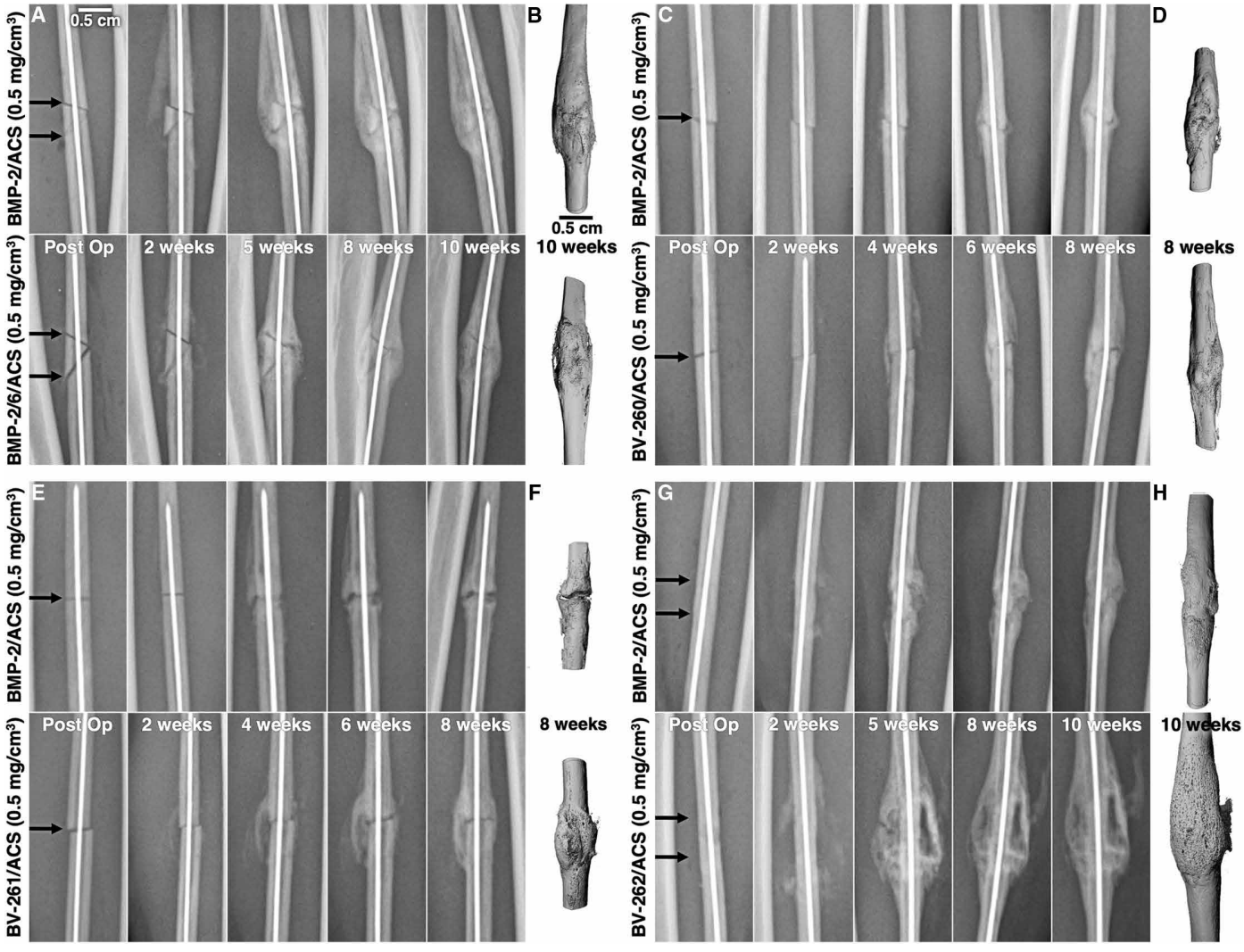

Fig. 4. Evaluation of BMP-2, BMP-2/6, BV-260, BV-261, and BV-262/ACS in macaque fibula osteotomy models. (**A**, **C**, **E**, and **G**) Radiographic time series and (**B**, **D**, **F**, and **H**) corresponding ex vivo μCT images of representative macaque bilateral fibula 0.5-cm wedge osteotomies treated with BMP-2/ACS (0.5 mg/cm^3) on one side and BMP-2/6/ACS (0.5 mg/cm^3) on the contralateral side (10 weeks; $n = 6$), bilateral 1-mm fibula transverse osteotomies treated with BMP-2/ACS (0.5 mg/cm^3) on one side and BV-260/ACS (0.5 mg/cm^3) on the contralateral side (8 weeks; $n = 6$), bilateral 1-mm fibula osteotomies treated with BMP-2/ACS (0.5 mg/cm^3) on one side and BV-261/ACS (0.5 mg/cm^3) on the contralateral side (8 weeks; $n = 7$), and bilateral fibula 0.5-cm wedge osteotomies treated with BMP-2/ACS (0.5 mg/cm^3) on one side and BV-262/ACS (0.5 mg/cm^3) on the contralateral side (10 weeks; $n = 6$). Black arrows locate the position of the osteotomy immediately after surgery (Post Op).

and Table 3). The retention profile of BMP-2/CPM was previously determined to be optimal for bone formation in nonhuman primates based on minimal initial burst release and subsequent prolonged retention (*17*). Similar retention profiles, $t_{1/2}$, and AUC for ^{125}I-labeled BV-265 loaded directly onto the CDHA granules and ^{125}I-labeled BV-265/CM support the primary role of the CDHA granules in determining BV-265 retention compared to the rhCollagen component of the CM.

The CDHA granules provide compression resistance, meeting the second carrier design criterion. The CM compressive strength and Young's modulus were significantly greater than ACS, composed of bovine collagen alone (Table 4). The combination of PGLA mesh and rhCollagen coating improved the handling properties of the CM, meeting the third design criterion. The CM ultimate tensile strength and Young's modulus were significantly greater than the CM without the polymer mesh and ACS (Table 4). Tensile mechanical properties of the CM without the mesh and ACS were similar. The rhCollagen coating limited granule shedding during surgical manipulation (fig. S23).

BV-265/CM induces larger intramuscular bone nodules in the rats compared to BMP-2/CM and CM alone in a dose-dependent manner

Histological evaluation of explants from CM-treated rats demonstrated residual CDHA granules and rhCollagen fibers imbedded in a dense connective tissue with no evidence of bone at 14 days (Fig. 6H and fig. S24A). BV-265/CM–treated implants induced bone ingrowth and a dose-dependent increase in explant nodule area and bone area/explant nodule area, meeting the fourth design criterion (Fig. 6, I to K; fig. S24, B to D; and Table 5). Trabecular bone was present in the vascularized connective tissue surrounding residual CDHA

Table 2. Torsional biomechanical measurements of the cynomolgus macaque bilateral fibula osteotomy models. Values presented as means ± SD. Mean values not sharing the same letter are significantly different ($P < 0.05$). Torsional mechanical properties data and equal variance paired two-tailed *t* test *P* values in data file S1. Torsional mechanical properties data and ANOVA group effect *P* values for all comparisons in data file S1. Tukey HSD post hoc test individual comparisons *P* values in data file S1.

Comparison	Model (no. of animals)	Duration (weeks)	Nonunion	Callus volume (mm^3)	Torsional stiffness (Nm/degree) (% intact fibulae)	Maximum torque (Nm) (% intact fibulae)
BMP-2/ACS (0.5 mg/cm^3)	Wedge (6)	10	3/6	869.1 ± 342.9^{A}	$0.043 \pm 0.032^{A,*}$ 68.5%	$0.92 \pm 0.36^{A,*}$ 44.2%
BMP-2/6/ACS (0.5 mg/cm^3)			3/6	847.9 ± 213.1^{A}	$0.031 \pm 0.017^{A,*}$ 64.9%	$0.87 \pm 0.23^{A,*}$ 31.9%
BMP-2/ACS (0.5 mg/cm^3)	Transverse (6)	8	4/6	438.9 ± 265.4^{A}	$0.041 \pm 0.024^{A,*}$ 56.1%	$0.75 \pm 0.29^{A,*}$ 44.1%
BV-260/ACS (0.5 mg/cm^3)			4/6	454.9 ± 300.3^{A}	$0.032 \pm 0.013^{A,*}$ 51.7%	$0.69 \pm 0.24^{A,*}$ 32.5%
BMP-2/ACS (0.5 mg/cm^3)	Transverse (7)	8	4/7	378.4 ± 110.6^{A}	$0.029 \pm 0.012^{A,*}$ 30.4%	$0.65 \pm 0.15^{A,*}$ 48.8%
BV-261/ACS (0.5 mg/cm^3)			6/7	572.8 ± 178.2^{B}	$0.044 \pm 0.018^{A,*}$ 45.8%	$0.82 \pm 0.29^{A,*}$ 60.9%
BMP-2/ACS (0.5 mg/cm^3)	Wedge (6)	10	6/6	876.8 ± 182.5^{A}	$0.048 \pm 0.019^{A,*}$ 50.2%	$0.92 \pm 0.20^{A,*}$ 68.4%
BV-262/ACS (0.5 mg/cm^3)			6/6	$1{,}368.4 \pm 266.9^{B}$	0.063 ± 0.019^{B} 65.2%	1.17 ± 0.27^{B} 87.6%
BMP-2/CPM (1.5 mg/cm^3)	Wedge (6)	10	6/6	$1{,}227.2 \pm 280.3^{A}$	$0.053 \pm 0.021^{A,*}$ 55.1%	$0.89 \pm 0.20^{A,*}$ 66.3%
BV-262/CPM (0.5 mg/cm^3)			6/6	$1{,}219.9 \pm 174.0^{A}$	$0.055 \pm 0.019^{A,*}$ 57.3%	$0.89 \pm 0.37^{A,*}$ 66.7%
BV-262/CPM (0.5 mg/cm^3)	Oblique (8)	8	7/8	$1{,}244.2 \pm 280.3^{A}$	$0.049 \pm 0.025^{A,*}$ 50.4%	$0.71 \pm 0.33^{A,*}$ 52.9%
BV-265/CPM (0.5 mg/cm^3)			8/8	$1{,}329.7 \pm 240.1^{A}$	0.067 ± 0.025^{B} 69.2%	1.10 ± 0.22^{B} 81.9%
Intact fibulae	(24)				0.096 ± 0.027	1.34 ± 0.27

*Torsional mechanical properties significantly different from intact fibulae ($P < 0.05$).

granules and rhCollagen fibers. Fenestrations and rhCollagen matrix macroporosity facilitated guided bone ingrowth, allowing blood vessels and cells access into the CM.

Histological evaluation of BV-265/CM–treated implants (11.3 μg) (Fig. 6, L to O, and figs. S24D and S25, A to D) and the CM implants (fig. S25E) demonstrated minimal inflammatory cellular infiltrate. Appositional bone formation on rhCollagen fibers was noted in the BV-265/CM–treated explants. Multinucleated tartrate-resistant acid phosphatase (TRAP)–positive stained osteoclasts were present, resorbing the surfaces of the CDHA granules in CM explants at day 14 (fig. S25F). rhCollagen was selected for reduced immunogenicity (*57*) and increased manufacturing uniformity (*58*) compared to extracted animal-derived collagen. These results confirm that the CM is both biocompatible and biodegradable, meeting the fifth design criterion. Histological evaluation of the paired BMP-2 and BV-265/CM implants demonstrated that both cytokines induce endochondral bone nodules in a similar manner typical of BMPs (figs. S26 to S35 and "Histological evaluation of paired rat intramuscular BMP-2 and BV-265/CM–treated explants" section in the Supplementary Materials). BV-265/CM–treated explants had greater explant nodule area compared to BMP-2/CM at 14 days (Table 5).

Combining BV-265 and the CM in translational studies

In silico analysis and $CD4^+$ T cell proliferation/interleukin-2 (IL-2) induction responses predicted BV-262 and BV-265 to have low immunogenicity, similar to that observed for BMP-2 in human clinical trials ("Immunogenicity evaluation section in the Supplementary Materials", figs. S36 to S38, and table S3). The lack of activity in the $CD4^+$ T cell proliferation and IL-2 induction assays also predicted a low immunogenicity response to the CM type I rhCollagen (table S5).

BV-265/CM concentrations targeted for bone trauma human clinical trials were evaluated in the macaque fibula 2-cm critical-sized ostectomy model (Fig. 7 and figs. S39 to S44). Untreated ostectomies failed to bridge at 12 weeks (Fig. 7A). Radiographs of the CM-treated ostectomies demonstrated progressive compression of the CM with no evidence of bridging (Fig. 7B). Ex vivo μCT and histology confirmed nonunion at 12 weeks (Fig. 7, C and D). The CM-treated ostectomies were filled with dense, minimally vascularized, connective tissue containing fibroblasts and stromal cell mixed lymphocytic/myeloid cell infiltrate surrounding residual CDHA granules (fig. S40). The BV-265/CM–treated ostectomies (0.05 mg/cm^3) demonstrated expansion of the CM and a progressive uniform increase in radiodensity consistent with bone bridging the defects between 8 and 12 weeks

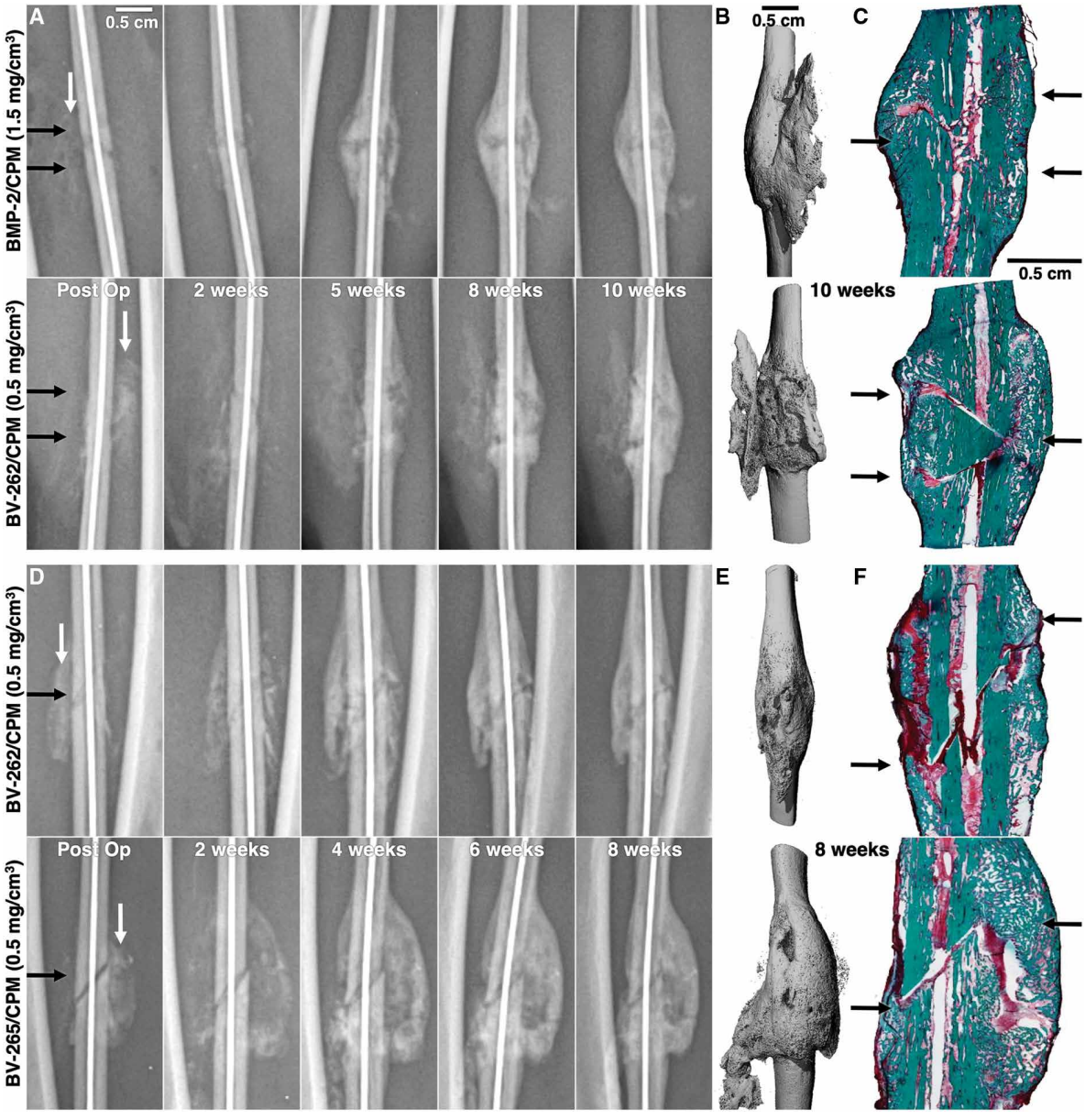

Fig. 5. Evaluation of BMP-2, BV-262, and BV-265/CPM in macaque fibula osteotomy models. (**A** and **D**) Radiographic time series, (**B** and **E**) corresponding ex vivo μCT images, and (**C** and **F**) histology (Goldner's trichrome stain) of representative macaque bilateral fibula 0.5-cm wedge osteotomies treated with BMP-2/CPM (1.5 mg/cm^3) on one side and BV-262/CPM (0.5 mg/cm^3) on the contralateral side (10 weeks; $n = 6$) and bilateral fibula 1-mm oblique osteotomies treated with BV-262/CPM (0.5 mg/cm^3) on one side and BV-265/CPM (mg/cm^3) on the contralateral side (8 weeks; $n = 8$). Radiodense CPM is visible immediately after surgery (Post Op, white arrows). Black arrows locate the position of the osteotomy.

(Fig. 7E). Ex vivo μCT and histology confirmed union of the ostectomies (Fig. 7, F and G). Uniform bone was present within a highly vascularized connective tissue surrounding the residual CDHA granules (figs. S41 and S42). BV-265/CM–treated ostectomies (0.15 mg/cm^3) demonstrated a rapidly forming peripheral radiodensity consistent with bone surrounding the expanded CM between 2 and 4 weeks (Fig. 7H). Radiographic bridging of the defects occurred between 8 and 12 weeks. Ex vivo μCT and histology confirmed union at 12 weeks (Fig. 7, I and J). A neocortex surrounding less mature, newly forming trabecular bone was observed within a vascularized connective tissue surrounding the residual CDHA granules (figs. S43 and S44). Osteoid on trabecular surfaces indicated ongoing remodeling/modeling in both treatment groups. Connective tissue surrounding the granules contained a combination of stromal cells and mixed lymphocytic/myeloid cells in the bridged BV-265/CM–treated ostectomies. TRAP-positive osteoclasts were observed resorbing residual CDHA granules in all three treatments (fig. S45). There was no evidence of residual rhCollagen at 12 weeks.

The CM-treated defects had significantly less mineralized volume, composed almost exclusively of residual CDHA granules, compared

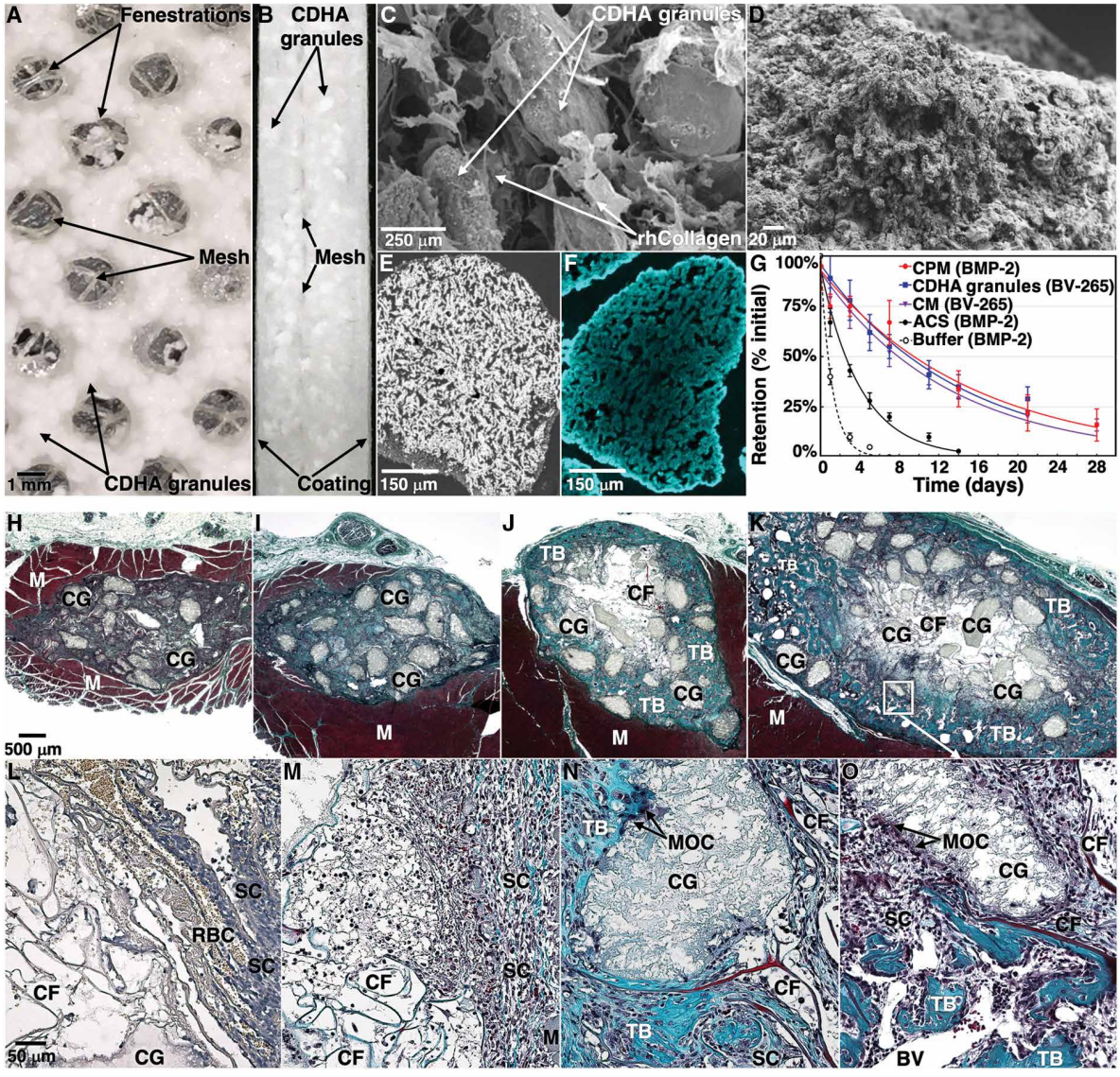

Fig. 6. CM components, cytokine retention profiles, and rat intramuscular explants. (**A**) CM composed of CDHA granules embedded in a fenestrated, polymer mesh–reinforced, macroporous rhCollagen matrix. (**B**) Top/bottom rhCollagen coating. (**C**) Scanning electron microscopy (SEM) image of CDHA granules within the macroporous rhCollagen matrix. (**D**) SEM image of a CDHA granule demonstrating high surface roughness. (**E**) SEM of a CDHA granule demonstrating internal interconnected porosity. (**F**) Fluorescence image of a sectioned CDHA granule demonstrating penetration of Alexa Fluor 488 fluorescent–conjugated BV-265 (cyan pseudo-color) into the interior of the granule. (**G**) In vivo retention of ^{125}I-labeled BV-265 delivered in CDHA granules and in the CM compared to ^{125}I-labeled BMP-2 implanted in CPM and ACS or injected in buffer into a rodent muscle pouch determined as a function of time (days). Data are means ± SD (n = 4 to 6 animals per group). (**H**) Histological evaluation of CM alone and (**I**) 0.45 μg, (**J**) 2.26 μg, and (**K**) 11.3 μg BV-265/CM–treated rat intramuscular implants at 14 days (Goldner's trichrome stain). Trabecular bone is visible in the 2.26 and 11.3 μg BV-265/CM–treated explants. Higher-magnification images of 11.3 μg BV-265/CM–treated explants at (**L**) 3 days, (**M**) 5 days, (**N**) 9 days, and (**O**) 14 days. M, muscle; CG, CDHA granules; CF, collagen fibers; RBC, red blood cells; SC, stromal cells; BV, blood vessels; MOC, multinucleated osteoclasts.

to the BV-265/CM–treated ostectomies at 12 weeks (Table 6). Callus volume was similar in both BV-265/CM–treated ostectomies. The untreated and CM-treated ostectomies were not amenable to torsional testing. Torsional stiffness of the BV-265/CM–treated ostectomies was similar. Torsional stiffness for BV-265/CM–treated ostectomies (0.05 and 0.15 mg/cm^3) was 34.2% and 65.3%, respectively, of the values for intact fibulae. Maximum torque of the BV-265/CM–treated ostectomies (0.15 mg/cm^3) was 47.9% greater than the value for the BV-265/CM–treated ostectomies (0.05 mg/cm^3) and was similar to the value for intact fibulae (77.5% of intact fibulae). Maximum torque for the BV-265/CM–treated ostectomies (0.05 mg/cm^3) was 52.4% of intact fibulae.

A baboon 2.5-cm fibula ostectomy model was used to evaluate longer-term remodeling in response to treatment with BV-265/CM (0.15 mg/cm^3) in larger fibulas compared to macaques. The BV-265 concentration was selected on the basis of superior mechanical properties in the macaque fibula ostectomy. Radiographic evaluation of the BV-265/CM–treated ostectomies demonstrated a progressive increase in radiodensity consistent with bone bridging the defects between 6 and 12 weeks (Fig. 8A and fig. S46). Additional remodeling/consolidation

Table 3. Comparison of BMP-2 and BV-265 retention in multiple carriers. AUC (fraction*days) = area under the % retention versus time curve for 0 to 7 days, 0 to 14 days, and 0 to 21 days. Individual data located in data file S1.

Treatment	$t_{1/2}$ (days)	$AUC_{0-7\ days}$ (fraction*days)	$AUC_{0-14\ days}$ (fraction*days)	$AUC_{0-21\ days}$ (fraction*days)	$AUC_{0-28\ days}$ (fraction*days)
BMP-2/buffer ($n = 4$)	0.71	1.40	–	–	–
BMP-2/ACS ($n = 4$)	2.69	3.03	3.29	–	–
BMP-2/CPM ($n = 6$)	8.12	5.12	8.66	10.64	11.95
BV-265/CDHA ($n = 3$)	5.14	5.18	8.22	10.46	–
BV-265/CM ($n = 4$)	6.03	4.89	7.65	9.39	10.67

Table 4. Mechanical properties of the CM and ACS. Values presented as means ± SD. Mean values not sharing the same letter are significantly different ($P < 0.05$). Compressive mechanical properties equal variance two-tailed t test ($P < 0.00001$). Tensile mechanical properties ANOVA group effect for all comparisons ($P < 0.00001$). Tukey HSD post hoc test CM containing mesh versus CM without mesh and ACS ($P < 0.0001$). CM without mesh and ACS ($P > 0.95$). Data and individual P values located in data file S1.

Carrier	No. per group	Strength* (kPa)	Modulus (kPa)
Compressive mechanical properties			
ACS	6	0.8 ± 0.2^{A}	3.6 ± 0.5^{A}
CM	9	82.7 ± 15.2^{B}	$1{,}402.4 \pm 195.0^{B}$
Tensile mechanical properties			
ACS	6	36.5 ± 5.0^{A}	103.9 ± 6.0^{A}
CM without a mesh	6	18.3 ± 2.7^{A}	94.8 ± 6.1^{A}
CM containing a mesh	6	262.5 ± 65.0^{B}	708.4 ± 98.1^{B}

*Compressive strength determined at 50% strain.

Table 5. Characterization of CM, BV-265/CM, and BMP-2/CM explants. Values presented as means ± SD. Mean values for the dose-ranging study and mean values for the paired BMP-2 versus BV-265/CM comparison not sharing the same letter are significantly different ($P < 0.05$) ($n = 4$ per group). Explant nodule area for the 0.0 μg group was the result of residual CDHA granules with no bone identified. ANOVA group effect for total explant nodule area and bone area/total explant nodule area ($P < 0.000003$ and $P < 0.00056$, respectively). Tukey HSD hoc test explant nodule area ($P < 0.05$) (group comparison P values in data file S1). Equal variance two-tailed paired t test explant 11.3 μg BMP-2 versus BV-265/CM area and bone area/explant area ($P < 0.045$ and $P > 0.006$). Individual data located in data file S1.

Treatment: Concentration (μg, mg/cm³)	Explant nodule area (mean ± SD)	Bone area/explant nodule area (mean ± SD)
BV-265/CM: 0.0 μg, 0.0 mg/cm³	$6.9 \pm 1.8\ mm^{2,A,B}$	$0.0 \pm 0.0\%^{A}$
BV-265/CM: 0.45 μg, 0.004 mg/cm³	$10.0 \pm 2.7\ mm^{2,B}$	$7.4 \pm 6.3\%^{A}$
BV-265/CM: 2.26 μg, 0.02 mg/cm³	$10.4 \pm 2.9\ mm^{2,B}$	$25.6 \pm 13.3\%^{B}$
BV-265/CM: 11.3 μg, 0.1 mg/cm³	$23.9 \pm 2.6\ mm^{2,C}$	$26.7 \pm 3.1\%^{B}$
BMP-2/CM: 11.3 μg, 0.1 mg/cm³	$12.5 \pm 4.3\ mm^{2,A}$	$35.8 \pm 0.1\%^{A}$
BV-265/CM: 11.3 μg, 0.1 mg/cm³	$20.7 \pm 4.3\ mm^{2,B}$	$31.8 \pm 0.1\%^{B}$

of the defect radiodensity occurred over the subsequent 26-week study. Ex vivo μCT and histology confirmed union at 26 weeks (Fig. 8, B and C, and figs. S47 and S48). A distinct cortex was present surrounding more uniform trabecular bone in a highly vascularized connective tissue surrounding the CDHA granules. Osteoid on trabecular surfaces and within the CDHA granules indicated ongoing bone and granule remodeling/modeling. TRAP-positive stained osteoclasts were observed resorbing both the surface and the interior of the macroporous CDHA granules (fig. S49). The vascularized connective tissue contained stromal cells and mixed lymphocytic/myeloid cells. There was no evidence of residual rhCollagen. Torsional stiffness was equivalent to the value for intact fibulae at 26 weeks (Table 6). Maximum torque was 53.5% greater than intact fibulae due to increased callus size and the method of mechanical testing.

A baboon fibula wedge osteotomy was used to simulate a clinically relevant three-part fracture. Radiographic evaluation of BV-265/CM–treated osteotomies (0.15 mg/cm³) demonstrated progressive increased radiodensity consistent with bone formation starting at 2 weeks (Fig. 8D). Radiographic bridging of the defects was present by 8 weeks. Consolidation/remodeling of the repair continued for the remaining 4 weeks. Ex vivo μCT and histology (Fig. 8, E and F) confirmed union of the osteotomies at 12 weeks. Similar to the BV-265/CM–treated defects, a dense peripheral neocortex surrounded more uniform bone within the highly vascularized connective tissue was observed surrounding residual CDHA granules (figs. S50 to S52). Osteoid on trabecular surfaces and within the CDHA granules indicated ongoing bone and granule remodeling/modeling. Multinucleated osteoclasts were resorbing the CDHA granules. Vascularized connective tissue contained stromal and mixed lymphocytic/myeloid cells. There was no evidence of residual rhCollagen. Torsional stiffness was 93.9% greater and maximum torque was 85.9% greater than intact fibulae (Table 6) because of increased callus size and method of mechanical testing.

No local or systemic adverse events were observed in any of the animals used in this study based on routine physical examination, hematology, implant histology, or gross postmortem evaluation.

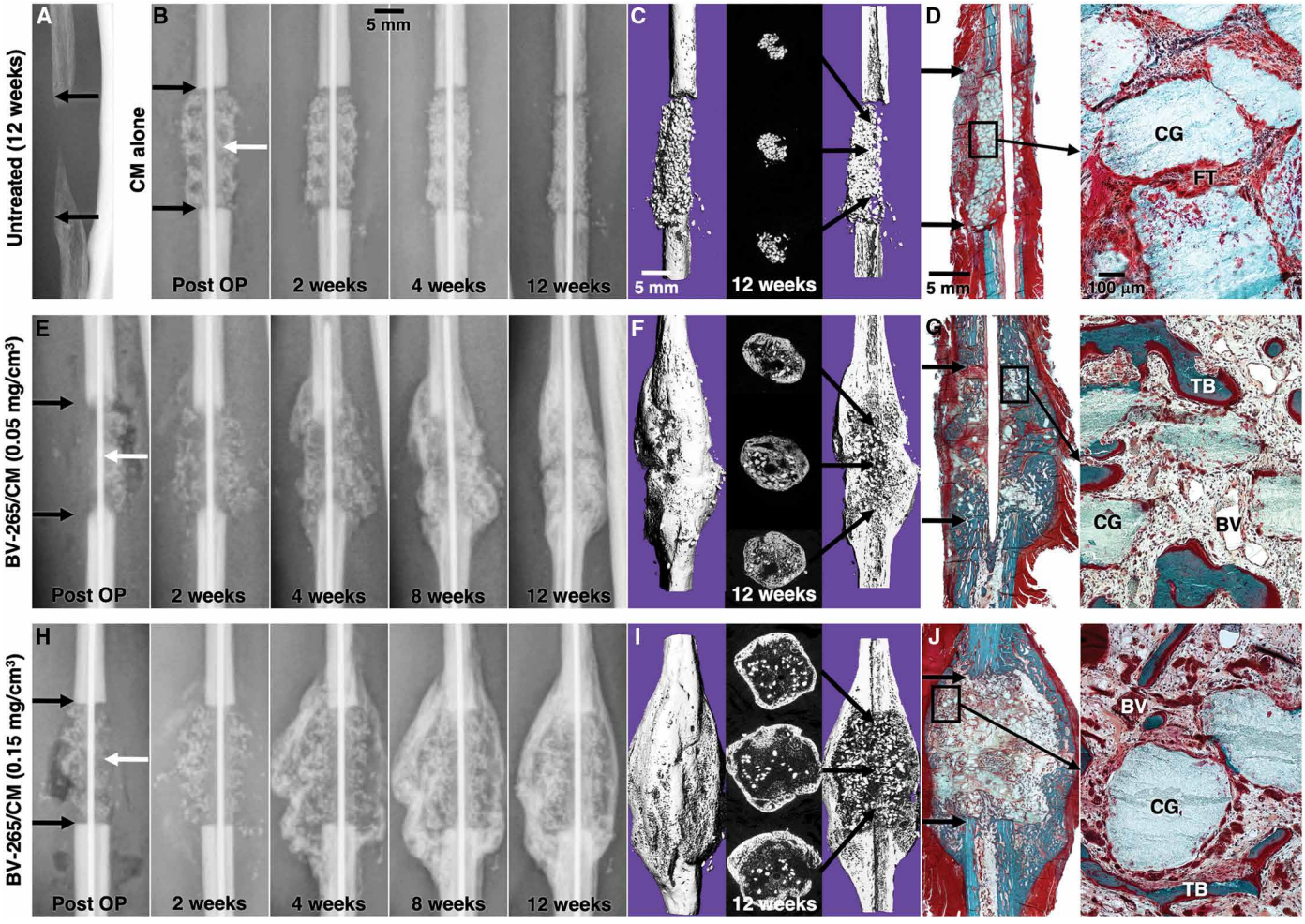

Fig. 7. Evaluation of BV-265/CM in a macaque fibula 2-cm critical-sized ostectomy. (**A**) Radiographic image of a representative untreated macaque 2-cm ostectomy demonstrating failure to bridge at 12 weeks ($n = 3$). (**B** to **D**) Radiographic time series, (**E** to **G**) μCT 3D reconstructions/slice images, and (**H** to **J**) histology (Goldner's trichrome stain) of a representative macaque 2-cm ostectomy treated with CM alone ($n = 3$), BV-265/CM (0.05 mg/cm^3), and BV-265/CM (0.15 mg/cm^3) ($n = 6$).

Exploratory toxicology evaluation of macaques and baboons treated with BV-265/CM found no gross or histological organ abnormities.

DISCUSSION

This study demonstrates the successful generation of an optimized BMP-2/BMP-6/activin A chimera/carrier for orthopedic reconstructive procedures. BV-265 met the predetermined cytokine design criteria of optimal BMP receptor binding and resistance to inhibition by noggin and gremlin. The results of the study confirm that BV-265 and the other chimeras are BMPs engaging BMP receptors, activating BMP downstream signaling components and target genes with superior potency/efficacy compared to BMP-2. Induction of ectopic bone in rodents, a unique property of BMPs, provides conclusive evidence that BV-265 engages BMP signaling components and demonstrates that BV-265–responsive cells are present. BV-265 induced superior bone formation when compared to BMP-2, BMP-2/6, and the other chimeric BMPs in a series of screening nonhuman primate fibula repair models. The CM consisting of CDHA granules suspended in a macroporous, fenestrated, polymer mesh–reinforced rhCollagen matrix and rhCollagen coating also met the predetermined design criteria. BV-265/CM demonstrated accelerated healing/remodeling in several translational nonhuman primate bone repair models at concentrations ranging from $^1/_{10}$ to $^1/_{30}$ of the BMP-2/ACS concentration (1.5 mg/cm^3) approved for clinical use in humans. Immunogenicity screening and evaluation of the study animals indicate that BV-265/CM appears safe, initiating no detectable local or systemic adverse events.

Improved efficacy of BV-265 in nonhuman primate bone repair models appears to result from the combination of all three cytokine design criteria. Low nanomolar affinity for ALK3, ALK6, and the BMP type II receptors, the first cytokine design criterion, did not result in BV-260 inducing superior repairs compared to BMP-2 at equivalent concentrations. Increased ALK2 binding alone, the second cytokine design criterion, resulted in BV-261 generating increased callus volume but not increased torsional mechanical properties compared to BMP-2. Combining design criteria one and two into a single chimera resulted in BV-262 generating increased callus volume and torsional mechanical properties compared to BMP-2 when both cytokines were administered at one-third the BMP-2/ACS concentration approved for clinical use in humans. Similar outcomes generated when BV-262 was administered at one-third the concentration and BMP-2 was

Table 6. Torsional biomechanical measurements of the nonhuman primate bilateral fibula ostectomy and osteotomy models. Values presented as means ± SD. Mean values not sharing the same letter are significantly different ($P < 0.05$). ANOVA group effect for macaque fibula ostectomy callus area ($P < 0.002$). Tukey HSD post hoc test ($P < 0.05$) (group comparison P values in data file S1). Equal variance paired two-tailed t test comparison of 0.05 versus 0.15 mg/cm^3 BV-265/CM torsional stiffness and maximum torque ($P > 0.10$ and $P < 0.016$, respectively). ANOVA group effect for macaque fibula ostectomy torsional stiffness and maximum torque versus intact fibulae ($P < 0.00002$). Tukey HSD post hoc test ($P < 0.05$) (group comparison P values in data file S1). Equal variance unpaired two-tailed t test comparison of baboon 2.5-cm ostectomy and baboon 1.0-cm wedge osteotomy BV-265/CM (0.15 mg/cm^3) versus intact fibulae torsional stiffness and maximum torque ($P > 0.65$ and $P < 0.001$, respectively, and $P > 0.0007$ and $P < 0.0009$, respectively). Individual data located in data file S1.

Treatment (mg/cm^3)	No. of animals	Duration (weeks)	Callus volume (mm^3)	Torsional stiffness (Nm/degree)	Maximum torque (Nm)
Macaque BV-265/CM 2.0-cm fibula ostectomy model					
Untreated defect	3	12	No bone present	Insufficient stiffness or strength to allow mechanical testing	
CM alone	3		133.7 ± 28.3^A		
BV-265/CM (0.05 mg/cm^3)	6 (bilateral)	12	422.8 ± 211.1^B	0.033 ± 0.019^{A,*}	0.70 ± 0.12^{A,*}
BV-265/CM (0.15 mg/cm^3)			573.8 ± 43.2^B	0.063 ± 0.024^{A,*}	1.04 ± 0.24^B
Intact macaque fibulae				0.096 ± 0.027	1.34 ± 0.27
Baboon BV-265/CM 2.5-cm fibula ostectomy model					
BV-265/CM (0.15 mg/cm^3)	6	26		0.188 ± 0.108	4.13 ± 0.56*
Baboon BV-265/CM bilateral 1.0-cm fibula wedge osteotomy model					
BV-265/CM (0.15 mg/cm^3)	3 (bilateral)	12		0.316 ± 0.046*	5.62 ± 1.27*
Intact baboon fibulae	5			0.163 ± 0.056	2.69 ± 0.47

*Significantly different from intact fibulae.

administered at the approved concentration for clinical use in humans confirm equivalent efficacy to BMP-2 at the lower BV-262 concentration. Combining the third design criterion, decreased sensitivity to extracellular BMP antagonists noggin and gremlin and the associated picomolar type II receptor binding affinity, with the first two design criteria into a single chimera resulted in BV-265 generating increased callus volume and superior torsional mechanical properties compared to BV-262 when both cytokines were administered at equivalent low concentrations.

The second design criterion, increased ALK2 binding, was achieved by BMP-2 tethers anchoring the amino acid sequences from the PHL and α-helix 3, involved in BMP type I receptor binding, from BMP-6 to BMP-2 (Fig. 1, A and F, and fig. S1F). Loss of ALK2 binding and the associated decrease in BV-261 ALP activity after partial deglycosylation confirm that increased BV-261/ALK2 binding was the direct result of the tethered glycan compared to BMP-6. The mechanism involved may include changes in PHL flexibility/conformation, producing a more favorable BV-261/ALK2 interface. The tethered glycan may also further stabilize the first GlcNAc monosaccharide of BV-261 critical for enhanced glycosylated BMP-6/ALK2 binding by direct interaction with ALK2 (*36*) or other mechanisms. Additional mechanisms summarized in the Supplementary Materials may contribute to increased BV-261, BV-262, and BV-265 binding to ALK2 compared to BMP-2, BMP-6, and BMP-7.

The third design criterion, reduced inhibition by extracellular BMP antagonists noggin and gremlin, was achieved by substituting the C-terminal amino acid sequences from activin A into BV-265. Noggin binds primarily to the C-terminal type II receptor binding domains of BMPs with a short N-terminal extension into the BMP type I receptor binding domain. Noggin acts as a soluble decoy receptor preventing BMPs from interacting with cell surface receptors (*2*, *27*, *28*). Activin A does not bind noggin. The activin A/type II receptor binding interface overlaps with the BMP/type II receptor binding interface in the C-terminal type II receptor binding domains involved in receptor/noggin binding (*30*). However, unlike activin A, substituting the C-terminal type II receptor binding region of activin A into BV-265 did not prevent noggin binding. This is likely due to the presence of the substituted BMP-6 amino acid sequences in the first finger type II binding domain of BV-265 compared to activin A. The observed reduced inhibition of BV-265 by noggin is likely related to the picomolar binding affinity of BV-265 for the type II receptors preferentially favoring BV-265 binding to precursor cell type II receptors over nanomolar binding to noggin. The mechanism of gremlin inhibition of BMP activity appears to be distinct for other BMP inhibitors and not well characterized (*53*).

In addition to reduced noggin inhibition, the BV-265 activin A–like picomolar type II receptor binding affinity likely also directly contributes to the increased efficacy of BV-265 compared to BMP-2. BMP-2 signaling has been reported to be primarily initiated by ligand binding to a single high-affinity type I receptor compared to initial binding to the lower affinity type II receptor based on differences in their associated complex half-life (*31*). The stability of this initial membrane binding event then allows sequential recruitment of additional receptors. Low-affinity type II receptors can be recruited into the complex owing to increases in avidity resulting from ligand binding to multiple membrane-bound receptors. The minimal complex

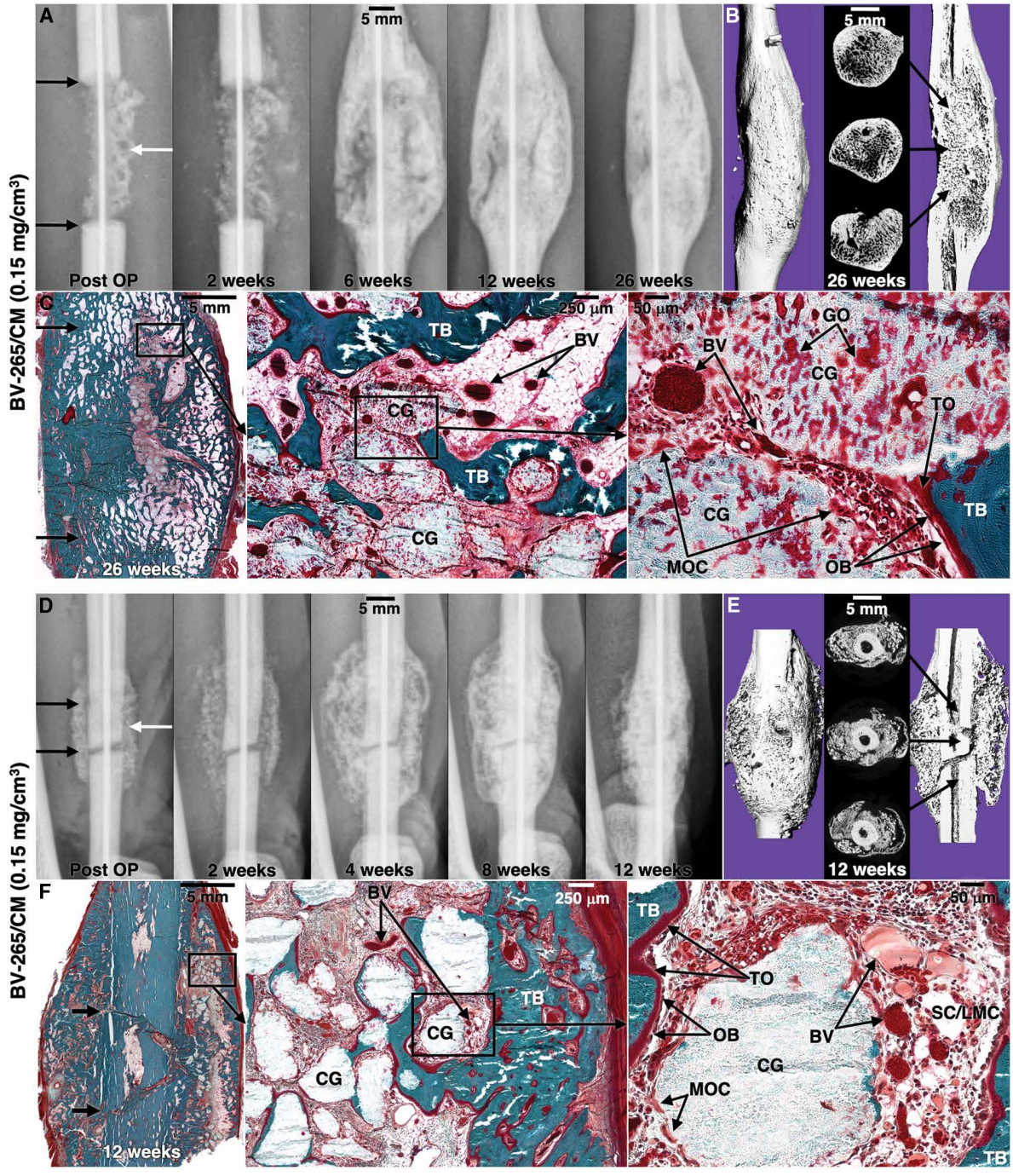

Fig. 8. Evaluation of BV-265/CM in baboon fibula 2.5-cm critical-sized ostectomy and fibula wedge osteotomy models. (**A** and **D**) Radiographic time series, (**B** and **E**) μCT 3D reconstructions/slice images, and (**C** and **F**) histology (Goldner's trichrome stain) of a representative baboon fibula 2.5-cm ostectomy treated with BV-265/CM (0.15 mg/cm^3, 26 weeks; $n = 6$) and a representative baboon fibula 1.0-cm wedge osteotomy treated with BV-265/CM (0.15 mg/cm^3, 12 weeks; $n = 6$). OB, osteoblasts; TO, trabecular osteoid; GO, granule osteoid.

for BMP-2 signaling has been reported to consist of one type I receptor and two type II receptors per ligand dimer (*31*, *32*). These results suggest that the limiting step in BMP-2 signaling appears to be recruitment of the low-affinity type II receptors. Acquisition of activin A–like picomolar type II receptor binding affinity likely negates this limiting step, allowing signaling at much lower BV-265 concentrations compared to BMP-2. Increased efficacy may also result from BV-265 picomolar type II receptor binding, limiting activin inhibition due to competition for shared type II receptors (*28*, *39*).

AB204, a BMP-2/activin A chimera containing amino acid substitutions from activin A into the β3-β5 finger 1 and β6-β9 C-terminal finger 2 regions of BMP-2, demonstrated similar reduced inhibition

by noggin and activin-like picomolar type II receptor binding but reduced binding to ALK3 compared to BMP-2 (*45*). AB204 demonstrated superior efficacy to BMP-2 in rodent calvarial and tibia bone repair models and in a canine posterolateral spine fusion model (*59*) at concentrations significantly lower than BMP-2. Evaluation of AB204 in translational nonhuman primate bone repair models has not been published. Structure-guided mutagenesis (I103Y) of AB204 increased ALK3 binding and osteogenic potency in cell-based assays. However, there are no published reports evaluating AB204 (I103Y) in animal models. Unlike BV-265, *Escherichia coli*–derived nonglycosylated AB204 and AB204 (I103Y) likely have nondetectable binding affinity for ALK2 similar to BMP-2.

Although the amino acid sequence of BV-265 differs from naturally occurring BMPs, both the in silico analysis and $CD4^+$ T cell proliferation and IL-2 induction responses predict a low immunogenicity response to BV-262 and BV-265, similar to the low immunogenicity response observed for BMP-2 in human clinical trials. The low immunogenicity potential is likely due to the combination of highly conserved amino acid sequences between BMP-2, BMP-6, and the chimeras as well as the selection of naturally occurring transitions between parental and substituted sequences into BV-262 and BV-265.

Transient bone resorption, heterotopic bone formation, and other local and systemic adverse events have been linked to rapid release of BMP-2 from ACS (*13*, *25*, *26*, *41*). The combination of substantially lower BV-265 concentrations delivered in the CM with improved BV-265 retention has the potential to limit both local and systemic adverse events. In addition, the lack of any activity in the $CD4^+$ T cell proliferation and IL-2 induction assays predicts a low immunogenicity response to the type I rhCollagen in the CM. Bovine-derived type I atelocollagen in the ACS carrier elicited significant antibody responses in some patients in human clinical trials. However, there was no apparent effect on BMP-2/ACS efficacy (*20*, *22*, *25*, *26*).

Limitations of this study include the lack of a crystal structure for the BV-261, BV-262, or BV-265/ALK2 complex to determine the mechanisms for increased ALK2 binding. In vivo identification of the specific cells responding to BV-265/CM at the repair site, characterization of their BMP receptor repertoire, and identification of the specific pathways activated in these cells were not determined. Considerable difficulty exists in performing these types of in vivo studies and interpreting the results from the complex repair environment in the more relevant nonhuman primate models compared to rodents. In addition, the relative contribution of potential responding cells in bone repair from the periosteum, bone marrow, muscle/fascia, and vasculature, particularly in severe trauma, the target of this study, remains uncertain. As an alternative, BMP receptor repertoire was determined from bone and muscle samples obtained from multiple species including nonhuman primates and humans. BMP receptor expression and BMP pathway activation were also confirmed in vitro in multiple cell types likely to participate in bone repair. In vivo activation of canonical BMP Smad signaling in rodents was also demonstrated in response to chimera treatment. BV-265/CM induced ectopic bone in rodents and bridged critical-sized bone defects in nonhuman primates, both of which are hallmarks of activated BMP signaling in BMP-responsive repair cells (*2*–*5*). Successful bone repair in nonhuman primates is also the most relevant outcome measure for translational studies evaluating therapies to augment fracture repair in humans. An additional potential limitation is translation of efficacious concentrations of BMPs determined in nonhuman primate orthopedic models to humans. Comparison of clinical trial and nonhuman primate studies evaluating BMP-2/carrier combinations for orthopedic and spine indications validates the translation of efficacious BMP/carrier concentrations determined in nonhuman primates to humans (*20*, *22*, *25*, *26*). Similar reliance on ALK2 in nonhuman primates and humans compared to other animal species suggested by relative BMP receptor expression in bone and muscle provides additional support for the translational role of nonhuman primate models of bone repair in predicting efficacy in humans. Despite these limitations, the results of this study support the use of BV-265/CM in human bone repair clinical trials at substantially lower concentrations than are currently approved for use with BMP-2/ACS.

MATERIALS AND METHODS

Study design

The objective of this study was to develop a next-generation BMP/carrier combination as an adjunct to surgical treatment of severe open fractures. Chimeric BMPs were engineered to meet specified cytokine design criteria of increased chimera BMP receptor binding. Crystal structure analysis, deglycosylation studies, and modeling of the putative BMP type I receptor binding interfaces were used to characterize potential mechanisms responsible for increased chimera/ALK2 receptor binding. Chimera BMP versus activin A/TGF-β, pSmad, and pp38 signaling was evaluated in murine and human cells. Osteogenic activity of the parental BMPs, BMP-2/6, and the chimeras was compared on the basis of ALP activity, and lead chimera osteogenic and angiogenic activity was assayed in human cells. Bone induction was assessed by injecting carrier-free formulations in a rat muscle pouch model. Area fraction of blood vessels was used to compare BV-265 and BMP-2 angiogenesis. BMP-2, BMP-2/6, and the chimeras were then screened for efficacy in established cynomolgus macaque fibula osteotomy repair models (table S2) (*17*, *56*). BV-265, a BMP-2/6/activin A chimera, was selected as the lead chimera based on the results of these evaluations. A CM composed of CDHA granules suspended in a macroporous, fenestrated, polymer mesh–reinforced rhCollagen matrix with a rhCollagen coating was also developed to meet the previously stated carrier design criteria. In vivo retention profiles of radiolabeled BV-265 and BMP-2 in various carriers were determined using intramuscular implantation in rodents. The rodent muscle pouch assay was used to determine compression resistance, handling properties, and the ability of increasing concentrations of BV-265/CM to induce bone formation. Last, a series of translational studies was performed to evaluate BV-265/CM for use in human fracture repair clinical trials. The potential for BV-265, BV-262, and CM rhCollagen to induce immunogenicity in humans was determined in silico and with $CD4^+$ T cell assays. BV-265/CM was tested in macaque and baboon fibula bone repair models. The Institutional Care and Use Committee approved protocols. All procedures were performed according to Association for Assessment and Accreditation of Laboratory Animal guidelines. Treatment allocation in the animal studies was determined by the study director before initiating the study. Most of the animal studies compared two treatments or treatment versus control in the same animal. Treatment allocation was not specifically randomized to right or left side or to individual animals in cases where single treatments were evaluated. The surgery and technical staff were unaware of the treatment allocation. Study outcomes were determined on the basis of animal numbers and/or right versus left limb, where applicable. Study outcomes

were matched to treatment after determination by the study director.

Statistical analysis

Unless otherwise noted, data were reported as means ± SD. Figure error bars are given as SD. Individual datasets used to generate mean values are reported in data file S1. Pairwise comparisons were evaluated using equal variance two-tailed paired *t* test. Unpaired comparisons were evaluated using equal variance two-tailed *t* test. Multiple comparisons were evaluated using one-way ANOVA. Tukey HSD post hoc test was performed when a significant ANOVA group effect was found. Nonparametric multiple comparisons were evaluated using Kruskal-Wallis rank sum test. The Dunn post hoc test was performed when a significant Kruskal-Wallis rank sum test group effect was found. A P value of ≤ 0.05 was considered as significant for all evaluations. Group sample sizes are reported in their respective figure caption(s) and table(s) and/or in Supplementary Materials and Methods. Sample size for animal studies was determined on the basis of previous publications by the authors, allowing detection of a significant difference in mean values at a power of 0.80 and an α of 0.05.

SUPPLEMENTARY MATERIALS

stm.sciencemag.org/cgi/content/full/11/489/eaar4953/DC1

Materials and Methods

Fig. S1. Amino acid sequence alignment of BMP-2, BMP-6, activin A, and chimera monomers and their corresponding ribbon structures.

Fig. S2. BMPs and chimera amino acid sequence and corresponding C2C12 ALP activity EC_{50}.

Fig. S3. Expression of BMP type I and II receptors in human, nonhuman primate, canine, rat, and mouse bone and muscle.

Fig. S4. BMP-2 and BV-265 heparin binding.

Fig. S5. Ribbon diagram of glycosylated BMP-2 and BMP-6.

Fig. S6. SDS-PAGE analysis of BMP-2 and BV-261 and the role of glycosylation in increased BV-261/ALK2 binding.

Fig. S7. BMP and BV-261 monomer surface charge diagrams and their corresponding glycans superimposed on ALK3 ribbon diagrams.

Fig. S8. Chimera/noggin binding and the effect of gremlin on BMP/chimera-induced ALP activity.

Fig. S9. BMP versus activin A/TGF-β signaling in C2C12 cells.

Fig. S10. BMP versus activin A/TGF-β signaling in hMSCs.

Fig. S11. BMP receptors in hPDCs and BMP versus activin A/TGF-β signaling in hPDCs and hMSCs.

Fig. S12. Cytokine-induced C2C12 CAGA-luciferase and HEK-Blue TGF-β SEAP activity.

Fig. S13. Smad 1/5/8 immunohistological staining of BMP-2– and BV-262/ACS–treated rat intramuscular explants.

Fig. S14. BMP-2, BMP-6, and BMP-2/6 activity in C3H10T$^1/_2$ cells and in a rat intramuscular explant.

Fig. S15. Angiogenic gene expression and secreted proteins in BMP and chimera-treated hMVECs and hPDCs.

Fig. S16. Receptor and osteogenic gene expression in BMP and chimera-treated hUVECs and hMVECs.

Fig. S17. BV-265/buffer–treated rat intramuscular explant.

Fig. S18. BMP-2/buffer–treated rat intramuscular explant.

Fig. S19. Endochondral and direct bone formation induced by BV-265/buffer in a rat intramuscular explant.

Fig. S20. Bone nodule vascular support in a BV-265/buffer–treated rat intramuscular explant.

Fig. S21. Vascular support in a BMP-2/buffer–treated rat intramuscular explant.

Fig. S22. Histological appearance of BMP-2/ACS–treated versus BMP-2/6/ACS–treated and BMP-2/ACS–treated versus BV-262/ACS–treated nonhuman primate fibula osteotomies.

Fig. S23. Granule shedding in an uncoated and a rhCollagen-coated CM.

Fig. S24. Histological appearance of CM alone and BV-265/CM–treated rat intramuscular implants.

Fig. S25. Time course histological appearance of 11.3 μg BV-265/CM and CM–treated rat intramuscular implants.

Fig. S26. Histological evaluation of a BMP-2/CM–treated rat intramuscular implant 1 day after treatment.

Fig. S27. Histological evaluation of a BV-265-2/CM–treated rat intramuscular implant 1 day after treatment.

Fig. S28. Histological evaluation of a BMP-2/CM–treated rat intramuscular implant 3 days after treatment.

Fig. S29. Histological evaluation of a BV-265/CM–treated rat intramuscular implant 3 days after treatment.

Fig. S30. Histological evaluation of a BMP-2/CM–treated rat intramuscular implant 5 days after treatment.

Fig. S31. Histological evaluation of a BV-265/CM–treated rat intramuscular implant 5 days after treatment.

Fig. S32. Histological evaluation of a BMP-2/CM–treated rat intramuscular implant 9 days after treatment.

Fig. S33. Histological evaluation of a BV-265/CM-treated rat intramuscular implant 9 days after treatment.

Fig. S34. Histological evaluation of a BMP-2/CM-treated rat intramuscular implant 14 days after treatment.

Fig. S35. Histological evaluation of a BV-265/CM-treated rat intramuscular implant 14 days after treatment.

Fig. S36. Analysis of the BMP-2 sequence using iTope.

Fig. S37. Analysis of the BV-262 sequence using iTope.

Fig. S38. Analysis of the BV-265 sequence using iTope.

Fig. S39. CM implanted in a cynomolgus macaque fibula 2-cm ostectomy.

Fig. S40. Histological appearance of a CM-treated macaque fibula 2-cm ostectomy 12 weeks after treatment.

Fig. S41. Histological appearance of a BV-265/CM (0.05 mg/cm^3)–treated macaque fibula 2-cm ostectomy neocortex 12 weeks after treatment.

Fig. S42. Histological appearance of the medullary region of a BV-265/CM (0.05 mg/cm^3)–treated macaque fibula 2-cm ostectomy 12 weeks after treatment.

Fig. S43. Histological appearance of a BV-265/CM (0.15 mg/cm^3)–treated macaque fibula 2-cm ostectomy neocortex 12 weeks after treatment.

Fig. S44. Histological appearance of the medullary region of a BV-265/CM (0.15 mg/cm^3)–treated macaque fibula 2-cm ostectomy 12 weeks after treatment.

Fig. S45. Positive TRAP-stained osteoclasts in macaque fibula ostectomies.

Fig. S46. Radiographic time series of a baboon fibula 2.5-cm ostectomy treated with BV-265/CM (0.15 mg/cm^3).

Fig. S47. Histological appearance of a BV-265/CM (0.15 mg/cm^3)–treated baboon fibula 2.5-cm ostectomy neocortex 26 weeks after treatment.

Fig. S48. Histological appearance of the medullary region of a BV-265/CM (0.15 mg/cm^3)–treated baboon fibula 2.5-cm ostectomy 26 weeks after treatment.

Fig. S49. Positive TRAP-stained osteoclasts in baboon fibula ostectomies.

Fig. S50. Histological appearance of a BV-265/CM (0.15 mg/cm^3)–treated baboon fibula 2.5-cm ostectomy neocortex 12 weeks after treatment.

Fig. S51. Histological appearance of the medullary region of a BV-265/CM (0.15 mg/cm^3)–treated baboon fibula 2.5-cm ostectomy 12 weeks after treatment.

Fig. S52. Histological appearance of the wedge region of a BV-265/CM (0.15 mg/cm^3)–treated baboon fibula 2.5-cm ostectomy 12 weeks after treatment.

Table S1. Data processing, refinement statistics, and Procheck analysis for glycosylated BMP-2, BMP-6, and BV-261.

Table S2. Summary of nonhuman primate BMP/chimera comparisons.

Table S3. Cytokine CD4$^+$ T cell assays (50 patient donors).

Table S4. Collagen CD4$^+$ T cell assays (50 patient donors).

Data file S1. Individual datasets for included study data (Excel file).

REFERENCES AND NOTES

1. S. N. Khan, F. P. Cammisa Jr., H. S. Sandhu, A. D. Diwan, F. P. Girardi, J. M. Lane, The biology of bone grafting. *J. Am. Acad. Orthop. Surg.* **13**, 77–86 (2005).
2. T. Katagiri, T. Watabe, Bone morphogenetic proteins. *Cold Spring Harb. Perspect. Biol.* **8**, a021899 (2016).
3. K. Ruschke, C. Hiepen, J. Becker, P. Knaus, BMPs are mediators in tissue crosstalk of the regenerating musculoskeletal system. *Cell Tissue Res.* **347**, 521–544 (2012).
4. K. Tsuji, A. Bandyopadhyay, B. D. Harfe, K. Cox, S. Kakar, L. Gerstenfeld, T. Einhorn, C. J. Tabin, V. Rosen, BMP2 activity, although dispensable for bone formation, is required for the initiation of fracture healing. *Nat. Genet.* **38**, 1424–1429 (2006).
5. V. Chappuis, L. Gamer, K. Cox, J. W. Lowery, D. D. Bosshardt, V. Rosen, Periosteal BMP2 activity drives bone graft healing. *Bone* **51**, 800–809 (2012).
6. V. S. Salazar, S. Ohte, L. P. Capelo, L. Gamer, V. Rosen, Specification of osteoblast cell fate by canonical Wnt signaling requires BMP2. *Development* **143**, 4352–4367 (2016).
7. M. P. Khan, K. Khan, P. S. Yadav, A. K. Singh, A. Nag, P. Prasahar, M. Mittal, S. P. China, M. C. Tewari, G. K. Nagar, D. Tewari, A. K. Trivedi, S. Sanyal, A. Bandyopadhyay, N. Chattopadhyay, BMP signaling is required for adult skeletal homeostasis and mediates bone anabolic action of parathyroid hormone. *Bone* **92**, 132–144 (2016).
8. M. Bais, J. McLean, P. Sebastiani, M. Young, N. Wigner, T. Smith, D. N. Kotton, T. A. Einhorn, L. C. Gerstenfeld, Transcriptional analysis of fracture healing and the induction of embryonic stem cell-related genes. *PLOS ONE* **4**, e5393 (2009).

9. Y. Y. Yu, S. Lieu, C. Lu, T. Miclau, R. S. Marcucio, C. Colnot, Immunolocalization of BMPs, BMP antagonists, receptors, and effectors during fracture repair. *Bone* **46**, 841–851 (2010).
10. S. Lin, K. K. H. SvoBoda, J. Q. Feng, X. Jiang, The biological function of type 1 receptors of bone morphogenetic protein in bone. *Bone Res.* **4**, 16005 (2016).
11. T. Niikura, D. J. Hak, A. H. Reddi, Global gene profiling reveals a downregulation of BMP gene expression in experimental atrophic nonunions compared to standard healing fractures. *J. Orthop. Res.* **24**, 1463–1471 (2006).
12. P. Kloen, D. Lauzier, R. C. Hamdy, Co-expression of BMPs and BMP-inhibitors in human fractures and non-unions. *Bone* **51**, 59–68 (2012).
13. H. Seeherman, J. M. Wozney, Delivery of bone morphogenetic proteins for orthopedic tissue regeneration. *Cytokine Growth Factor Rev.* **16**, 329–345 (2005).
14. H. J. Seeherman, K. Azari, S. Bidic, L. Rogers, X. J. Li, J. O. Hollinger, J. M. Wozney, rhBMP-2 delivered in a calcium phosphate cement accelerates bridging of critical-sized defects in rabbit radii. *J. Bone Joint Surg. Am.* **88**, 1553–1565 (2006).
15. R. D. Welch, A. L. Jones, R. W. Buckholz, C. M. Reinert, J. S. Tjia, W. A. Pierce, J. M. Wozney, X. J. LI, Effect of recombinant human bone morphogenetic protein-2 on fracture healing in a goat tibial fracture model. *J. Bone Miner. Res.* **13**, 1483–1490 (1998).
16. M. F. Sciadii, K. D. Johnson, Evaluation of recombinant human bone morphogenetic protein-2 as a bone-graft substitute in a canine segmental defect model. *J. Orthop. Res.* **18**, 289–302 (2000).
17. H. Seeherman, R. Li, M. Bouxsein, H. Kim, X. J. Li, E. A. Smith-Adaline, M. Aiolova, J. M. Wozney, rhBMP-2/calcium phosphate matrix accelerates osteotomy-site healing in a nonhuman primate model at multiple treatment times and concentrations. *J. Bone Joint Surg. Am.* **88**, 144–160 (2006).
18. H. J. Seeherman, X. J. Li, E. Smith, J. M. Wozney, rhBMP-2/calcium phosphate matrix induces bone formation while limiting transient bone resorption in a nonhuman primate core defect model. *J. Bone Joint Surg. Am.* **94**, 1765–1776 (2012).
19. S. L. Salkfeld, L. P. Patron, R. L. Barrack, S. D. Cook, The effect of osteogenic protein-1 on the healing of segmental bone defects treated with autograft or allograft bone. *J. Bone Joint Surg. Am.* **83**, 803–816 (2001).
20. B. McKay, H. S. Sandhu, Use of recombinant human bone morphogenetic protein-2 in spine fusion applications. *Spine* **27**, S66–S85 (2002).
21. J. M. Toth, M. Wang, J. Lawson, J. M. Badura, K. B. DuBose, Radiographic, biomechanical, and histological evaluation of rhBMP-2 in a 3-level intertransverse process spine fusion: An ovine study. *J. Neurosurg. Spine* **25**, 733–739 (2016).
22. W. F. McKay, S. M. Peckham, J. M. Badura, A comprehensive clinical review of recombinant human bone morphogenetic protein-2 (INFUSE® bone graft). *Int. Orthop.* **31**, 729–734 (2007).
23. G. E. Friedlaender, C. R. Perry, J. D. Cole, S. D. Cook, G. Cierny, G. F. Muschler, G. A. Zych, J. H. Calhoun, A. J. LaForte, S. Yin, Osteogenic protein-1 (bone morphogenetic protein-7) in the treatment of tibial nonunions. *J. Bone Joint Surg. Am.* **83**, S151–S158 (2001).
24. J. R. Dimar II, S. D. Glassman, J. K. Burkus, P. W. Pryor, J. W. Hardacker, L. Y. Carreon, Clinical and radiographic analysis of an optimized rhBMP-2 formulation as an autograft replacement in posterolateral lumbar spine arthrodesis. *J. Bone Joint Surg. Am.* **91**, 1377–1386 (2009).
25. E. A. Barcak, M. J. Beebe, Bone morphogenetic protein. Is there still a role in orthopedic trauma in 2017? *Orthop. Clin. North Am.* **48**, 301–309 (2017).
26. G. S. Krishnakumar, A. Roffi, D. Reale, E. Kon, G. Filardo, Clinical application of bone morphogenetic proteins for bone healing: A systematic review. *Int. Orthop.* **41**, 1073–1083 (2017).
27. J. Nickel, W. Sebald, J. C. Groppe, T. D. Mueller, Intricacies of BMP receptor assembly. *Cytokine Growth Factor Rev.* **20**, 367–377 (2009).
28. D. Yadin, P. Knaus, T. D. Mueller, Structural insights into BMP receptors: Specificity, activation and inhibition. *Cytokine Growth Factor Rev.* **27**, 13–34 (2016).
29. G. P. Allendorph, M. J. Isaacs, Y. Kawakami, J. C. Izpisua Belmonte, S. Choe, BMP-3 and BMP-6 structures illuminate the nature of binding specificity with receptors. *Biochemistry* **46**, 12238–12247 (2007).
30. J. Greenwald, J. Groppe, P. Gray, E. Wiater, W. Kwiatkowski, W. Vale, S. Choe, The BMP7/ActRII extracellular domain complex provides new insights into the cooperative nature of receptor assembly. *Mol. Cell* **11**, 605–617 (2003).
31. K. Heinecke, A. Seher, W. Schmitz, T. D. Mueller, W. Sebald, J. Nickel, Receptor oligomerization and beyond: A case study in bone morphogenetic proteins. *BMC Biol.* **7**, 59 (2009).
32. M. J. Isaacs, Y. Kawakami, G. P. Allendorph, B. H. Yoon, J. C. Izpisua Belmonte, S. Choe, Bone morphogenetic protein-2 and -6 heterodimer illustrates the nature of ligand-receptor assembly. *Mol. Endocrinol.* **24**, 1469–1477 (2010).
33. S. R. Angle, K. Sena, D. R. Sumner, W. W. Virkus, A. S. Virdi, Healing of rat femoral segmental defect with bone morphogenetic protein-2: A dose response study. *J. Musculoskelet. Neuronal Interact.* **12**, 28–37 (2012).
34. G. J. Martin Jr., S. D. Boden, M. A. Morone, P. A. Moskovitz, Posterolateral intertransverse process spinal arthrodesis with rhBMP-2 in a nonhuman primate: Important lessons learned regarding dose, carrier and safety. *J. Spinal Disord.* **12**, 179–186 (1999).
35. S. Saremba, J. Nickel1, A. Seher, A. Kotzsch, W. Sebald, T. D. Mueller, Type I receptor binding of bone morphogenetic protein 6 is dependent on N-glycosylation of the ligand. *FEBS J.* **275**, 172–183 (2008).
36. K. Lavery, P. Swain, D. Falb, M. H. Alaoui-Ismaili, BMP-2/4 and BMP-6/7 differentially utilize cell surface receptors to induce osteoblastic differentiation of human bone marrow-derived mesenchymal stem cells. *J. Biol. Chem.* **283**, 20948–20958 (2008).
37. S. Shi, J. Cai, D. J. J. de Gorter, G. Sanchez-Duffhues, D. U. Kemaladewi, W. M. H. Hoogaars, A. Aartsma-Rus, P. A. C. 't Hoen, P. ten Dijke, Antisense-oligonucleotide mediated exon skipping in activin-receptor-like kinase 2: Inhibiting the receptor that is overactive in fibrodysplasia ossificans progressiva. *PLOS ONE* **8**, e69096 (2013).
38. M. Pacifici, E. M. Shore, Common mutations in ALK2/ACVR1, a multi-faceted receptor, have roles in distinct pediatric musculoskeletal and neural orphan disorders. *Cytokine Growth Factor Rev.* **27**, 93–104 (2016).
39. S. J. Hatsell, V. Idone, D. M. A. Wolken, L. Huang, H. J. Kim, L. Wang, X. Wen, K. C. Nannuru, J. Jimenez, L. Xie, N. Das, G. Makhoul, R. Chernomorsky, D. D' Ambrosio, R. A. Corpina, C. J. Schoenherr, K. Feeley, P. B. Yu, G. D. Yancopoulos, A. J. Murphy, A. N. Economides, *ACVR1*^{R206H} receptor mutation causes fibrodysplasia ossificans progressiva by imparting responsiveness to activin A. *Sci. Transl. Med.* **7**, 303ra137 (2015).
40. B. Bragdon, O. Moseychuk, S. Saldanha, D. King, J. Julian, A. Nohe, Bone morphogenetic proteins: A critical review. *Cell. Signal.* **23**, 609–620 (2011).
41. H. J. Seeherman, X. J. Li, M. L. Bouxsein, J. M. Wozney, rhBMP-2 induces transient bone resorption followed by bone formation in nonhuman primate core-defect model. *J. Bone Joint Surg. Am.* **92**, 411–426 (2010).
42. M. H. Alaoui-Ismaili, D. Falb, Design of second generation therapeutic recombinant bone morphogenetic proteins. *Cytokine Growth Factor Rev.* **20**, 501–507 (2009).
43. K. Schmidt-Bleek, B. M. Willie, P. Schwabec, P. Seemann, G. N. Duda, BMPs in bone regeneration: Less is more effective, a paradigm-shift. *Cytokine Growth Factor Rev.* **27**, 141–148 (2016).
44. J. W. Lowery, B. Brookshire, V. Rosen, A survey of strategies to modulate the bone morphogenetic protein signaling pathway: Current and future perspectives. *Stem Cells Int.* **2016**, 7290686 (2016).
45. B.-H. Yoon, L. Esquivies, C. Ahn, P. C. Gray, S. K. Ye, W. Kwiatkowski, S. Choe, An activin a/BMP2 chimera, AB204, displays bone-healing properties superior to those of BMP2. *J. Bone Min. Res.* **29**, 1950–1959 (2014).
46. E. Migliorinia, A. Valatc, C. Picartc, E. A. Cavalcanti-Adam, Tuning cellular responses to BMP-2 with material surfaces. *Cytokine Growth Factor Rev.* **27**, 43–54 (2016).
47. S. S. Lee, B. J. Huang, S. R. Kaltz, S. Sur, C. J. Newcomb, S. R. Stock, R. N. Shah, S. I. Stupp, Bone regeneration with low dose BMP-2 amplified by biomimetic supramolecular nanofibers within collagen scaffolds. *Biomaterials* **34**, 452–459 (2013).
48. R. Ruppert, E. Hoffman, W. Sebald, Human bone morphogenetic protein 2 contains a heparin-binding site which modifies its biological activity. *Eur. J. Biochem.* **237**, 295–302 (1996).
49. D. Weber, A. Kotzsch, J. Nickel, S. Harth, A. Seher, U. Mueller, W. Sebald, T. D. Mueller, A silent H-bond can be mutationally activated for high-affinity interaction of BMP-2 and activin type IIB receptor. *BMC Struct. Biol.* **7**, 6 (2007).
50. G. P. Allendorph, W. W. Vale, S. Choe, Structure of the ternary signaling complex of a TGF-β superfamily member. *Proc. Natl. Acad. Sci. U.S.A.* **103**, 7643–7648 (2006).
51. S. Keller, J. Nickel, J.-L. Zhang, W. Sebald, T. D. Mueller, Molecular recognition of BMP-2 and BMP receptor IA. *Nat. Struct. Mol. Biol.* **11**, 481–488 (2004).
52. T. Kirsch, W. Sebald, M. K. Dreyer, Crystal structure of the BMP-2-BRIA ectodomain complex. *Nat. Struct. Mol. Biol.* **7**, 492–496 (2000).
53. M. Kišonaitė, X. Wang, M. Hyvönen, Structure of gremlin-1 and analysis of its interaction with BMP-2. *Biochem. J.* **473**, 1593–1604 (2016).
54. A. Holtzhausen, C. Golzio, T. How, Y.-H. Lee, W. P. Schiemann, N. Katsanis, G. C. Blobe, Novel bone morphogenetic protein signaling through Smad2 and Smad3 to regulate cancer progression and development. *FASEB J.* **28**, 1248–1267 (2014).
55. A. Benn, C. Hiepen, M. Osterland, C. Schutte, A. Zwijsen, P. Knaus, Role of bone morphogenetic protein in sprouting angiogenesis: Differential BMP receptor-dependent signaling pathways balance stalk vs. tip cell competence. *FASEB J.* **31**, 4720–4733 (2017).
56. H. J. Seeherman, M. Bouxsein, H. Kim, R. Li, X. J. Li, M. Aiolova, J. M. Wozney, Recombinant human bone morphogenetic protein-2 delivered in an injectable calcium phosphate paste accelerates osteotomy-site healing in a nonhuman primate model. *J. Bone Joint Surg. Am.* **86**, 1961–1972 (2004).
57. O. Shoseyov, Y. Posen, F. Grynspan, Human recombinant type I collagen produced in plants. *Tissue Eng. Part A* **19**, 1527–1533 (2013).
58. H. Stein, M. Wilensky, Y. Tsafrir, M. Rosenthal, R. Amir, T. Avraham, K. Ofir, O. Dgany, A. Yayon, O. Shoseyov, Production of bioactive, post-translationally modified, heterotrimeric, human recombinant type-I collagen in transgenic tobacco. *Biomacromolecules* **10**, 2640–2652 (2009).
59. G. B. Zheng, B.-H. Yoon, J. H. Lee, Comparison of the osteogenesis and fusion rates between activin A/BMP-2 chimera (AB204) and rhBMP-2 in a beagle's posterolateral lumbar spine model. *Spine J.* **17**, 1529–1536 (2017).

Acknowledgments: We thank D. D. Augusta, D. Gavin, A. Hines, J. Kambouris, M. Lech, X. J. Li, A. Murphy, J. Yang, M. Wadanoli, and the Mannheimer Institute support staff for their help with in vivo and in vitro studies. We thank A. Pavesio, J. Welch, H. Tung, and Bioventus/Pfizer senior management for their support of this project. **Funding:** Funding was provided by Pfizer Inc. and Bioventus LLC. Materials were either exchanged via material transfer agreement between the institutions involved in this research or purchased from the involved institutions.
Author contributions: H.J.S. was the project leader participating in study design, chimera and CM design, surgery, data analysis, and manuscript preparation. S.P.B. and R.X.M. designed the chimeric proteins and participated in the study design. S.P.B. and K.E.T. performed biosensor studies. M.J.C. and J.G. performed in vitro characterization assays. C.T.B. produced chimera and BMP-2/6 cell lines and expressed, purified, and characterized these proteins. S.J. determined the crystal structure of BV-261, performed structural analysis, and generated BMP, activin A, and chimera ribbon diagrams. M.B. participated in the CDHA granule design and manufacturing. O.G., N.O., and O.S. were involved in rhCollagen and CM design and fabrication. S.J. designed and performed BMP receptor expression studies and data analysis. E.J.V. and C.G.W. participated in study design, characterization of the CM, retention profiles, and ALP activity assays and, along with P.R.M., were involved in animal studies and data analysis. J.E. and C.C. designed and executed the human cell-based assays. J.M.W. participated in the study design, data analysis, and interpretation. All of the authors reviewed the manuscript. **Competing interests:** S.P.B., R.X.M., M.J.C., J.M.W., H.J.S., Z.S.J., and C.T.B. are inventors on issued patents US8952131B2 and US9688735B2 held by Wyeth LLC covering designer osteogenic proteins. H.J.S., E.J.V., and M.B. are inventors on issued patent US10131543B2 held by Mathys AG Bettlach and Bioventus LLC covering methods for producing porous CDHA granules. O.G., N.O., H.J.S., O.S., E.J.V., C.G.W., and J.M.W. are inventors on the patent application US20170319750A1 held by CollPlant Ltd. and Bioventus LLC covering CMs designed for enhanced bone repair. J.M.W., H.J.S., C.T.B., and E.J.V. were formerly employed by Pfizer Inc. and Bioventus LLC. J.M.W. was a consultant for Bioventus LLC and is a consultant for SkelRegen. C.G.W. and J.G. are former employees of Bioventus LLC. S.P.B., M.J.C., Z.S.J., K.E.T., and R.X.M. are or were employees of Pfizer Inc. M.B. was an employee of Robert Mathys Stiftung (RMS) Foundation. N.O. and O.S. are employees of CollPlant Ltd. O.S. is a consultant to CollPlant Ltd. P.R.M. is an employee of the Mannheimer Foundation. All other authors declare that they have no competing interests. The research performed in this paper is related to the work performed by Pfizer Inc., Bioventus LLC, CollPlant Ltd., RMS Foundation, and Mannheimer Foundation. These institutions may benefit from this work. **Data and materials availability:** All summary data and individual measurements associated with this study are present in the paper or Supplementary Materials and data file S1. The chimeric BMPs, BMPs, and certain carrier materials described in this article may be obtained through a material transfer agreement with the authors and Bioventus.

Submitted 17 November 2017
Resubmitted 19 July 2018
Accepted 11 March 2019
Published 24 April 2019
10.1126/scitranslmed.aar4953

Citation: H. J. Seeherman, S. P. Berasi, C. T. Brown, R. X. Martinez, Z. S. Juo, S. Jelinsky, M. J. Cain, J. Grode, K. E. Tumelty, M. Bohner, O. Grinberg, N. Orr, O. Shoseyov, J. Eyckmans, C. Chen, P. R. Morales, C. G. Wilson, E. J. Vanderploeg, J. M. Wozney, A BMP/activin A chimera is superior to native BMPs and induces bone repair in nonhuman primates when delivered in a composite matrix. *Sci. Transl. Med.* **11**, eaar4953 (2019).

Science Translational Medicine

A BMP/activin A chimera is superior to native BMPs and induces bone repair in nonhuman primates when delivered in a composite matrix

Howard J. Seeherman, Stephen P. Berasi, Christopher T. Brown, Robert X. Martinez, Z. Sean Juo, Scott Jelinsky, Michael J. Cain, Jaclyn Grode, Kathleen E. Tumelty, Marc Bohner, Orly Grinberg, Nadav Orr, Oded Shoseyov, Jeroen Eyckmans, Christopher Chen, Pablo R. Morales, Christopher G. Wilson, Eric J. Vanderploeg and John M. Wozney

Sci Transl Med **11**, eaar4953.
DOI: 10.1126/scitranslmed.aar4953

Building better bone

Bone morphogenetic protein (BMP) can promote superior bone growth compared to autograft, historically considered the "gold standard" for bone repair; however, supraphysiologic concentrations of BMP are typically required. Seeherman *et al*. developed chimeric BMPs with improved potency and an optimized carrier matrix. Chimeras based on BMP-2 were engineered to express BMP-6 and activin A receptor binding domains, which improved binding affinity and activated BMP target genes in cells and resulted in greater bone formation in rats. Complete bone healing was observed in nonhuman primate models of open fracture using composite carrier to deliver concentrations of chimeric BMP that were lower than those approved for clinical use. This study systematically identifies an optimized BMP chimera and carrier combination with promising potential for bone healing.